UNIVERSITY OF THESSALY
SCHOOL OF ENGINEERING
DEPARTMENT OF MECHANICAL ENGINEERING

PARAMETER IDENTIFICATION OF PATIENT-SPECIFIC WINDKESSEL MODELS OF THE AORTA VIA PHYSICS-INFORMED NEURAL NETWORKS

by
GRAMMATIKAKIS GEORGIOS

Submitted in partial fulfillment of the requirements for the degree of Diploma in Mechanical Engineering at the University of Thessaly

Volos, 2025

UNIVERSITY OF THESSALY
SCHOOL OF ENGINEERING
DEPARTMENT OF MECHANICAL ENGINEERING

PARAMETER IDENTIFICATION OF PATIENT-SPECIFIC WINDKESSEL MODELS OF THE AORTA VIA PHYSICS-INFORMED NEURAL NETWORKS

by
GRAMMATIKAKIS GEORGIOS

Submitted in partial fulfillment of the requirements for the degree of Diploma in Mechanical Engineering at the University of Thessaly

Volos, 2025

Approved by the Committee on Final Examination:

Advisor Dr. Konstantinos Ampountolas,
Professor, Department of Mechanical Engineering,
University of Thessaly

Member Dr. Vasilios Bontozoglou,
Professor, Department of Mechanical Engineering,
University of Thessaly

Member Dr. Konstantinos Ritos,
Assistant Professor, Department of Mechanical Engineering,
University of Thessaly

Date Approved: [26/06/2025]

Ευχαριστίες

Ο συγγραφέας θα ήθελε να ευχαριστήσει την Αν. Καθηγήτρια Ασημίνα Καζακίδη και τον Δρ. Scott Black από το Πανεπιστήμιο του Strathclyde για την κοινοποίηση των δεδομένων, τη συζήτησή και επεξήγησή τους από την δημοσιευμένη εργασία τους SMD Black, C Maclean, P Hall Barrientos, K Ritos, A McQueen, A Kazakidi (2023), *Calibration of patient-specific boundary conditions for coupled CFD models of the aorta derived from 4D Flow-MRI.* Frontiers in Bioengineering and Biotechnology 11, 1178483. doi.org/10.3389/fbioe.2023.1178483

Acknowledgements

The author would like to thank Associate Professor Asimina Kazakidi and Dr. Scott Black from the University of Strathclyde for sharing the data, as well as for the discussion and explanation thereof, based on their published work SMD Black, C Maclean, P Hall Barrientos, K Ritos, A McQueen, A Kazakidi (2023), *Calibration of patient-specific boundary conditions for coupled CFD models of the aorta derived from 4D Flow-MRI.* Frontiers in Bioengineering and Biotechnology 11, 1178483. doi.org/10.3389/fbioe.2023.1178483

PARAMETER IDENTIFICATION OF PATIENT-SPECIFIC WINDKESSEL MODELS OF THE AORTA VIA PHYSICS-INFORMED NEURAL NETWORKS.

GRAMMATIKAKIS GEORGIOS
Department of Mechanical Engineering, University of Thessaly

Supervisor: Dr. Konstantinos Ampountolas

Abstract

Development in neural networks and specifically the incorporation of physical information via differential equations allows for estimation of patient-specific parameters for Windkessel models (2-, 3-, and 4-element). All the arterial models were applied on a type B aortic dissection patient's aorta, inserting each model's equations in a physics-informed neural network (PINN), along with pressure data from Nektar1D simulations and in-vivo flow measurements. Python's DeppXDE library was used to implement the inverse problem as well as design and train the PINN. It is shown that the parameters were estimated successfully, while being biologically consistent regarding physiological constraints, with the three-element Windkessel offering the best balance between accuracy and simplicity. Frequency response was also investigated for each model, creating Bode plots and testing the computed input impedances against the ones derived from the data. The combination of physics-based reasoning and machine learning proved to be a promising tool for parameter identification in cardiovascular modeling.

Key words: Windkessel, Parameters, Neural Network, Physics-Informed Neural Network, DeepXDE, Bode plot, Input Impedance, Architecture, Data, Element, Frequency Response.

Contents

List of Figures

List of Tables

1 Introduction

The aorta is the largest artery in the human body and plays a crucial role in systemic circulation and pressure damping. While investigating the aorta, it is common to focus on its five segments: RSA (Right Subclavian Artery), RCCA (Right Common Carotid Artery), LCCA (Left Common Carotid Artery), LSA (Left Sublcavian Artery), DAo (Descending Aorta); the brances that send blood to the rest of the body. RSA and LSA supply the arms, shoulders and part of the neck and brain, RCCA and LCCA focus more on the head and brain while DAo is responsible for the thoracic and abdominal organs, the spinal cord and the lower limbs. One of the most catastrophic cardiovascular diseases is aortic dissection, where the intima layer of the aorta tears and blood tracks through creating a false lumen. Type B aortic dissection is investigated where the tear is at the descending aorta, creating an extra segment and ultimately having DAoTL and DAoFL (true and false lumen) instead of just DAo. Arterial modeling is essential for diagnostics and simulations, as learning information in a non-invasive way in more practical, quicker and comes at a lower cost for both the patient and the expert. The lumped Windkessel models were used to depict all six segments of the aorta as electrical circuits and provided the equations required for the analysis. All the Windkessel models were tested: the simple 2-element proposed by Otto Frank, the intermediate 3-element adding characteristic impedance and the more complex 4-element models (parallel and in-series connection) modeling inertance as an inductor. The proposed method for estimating each model's parameters employs physics-informed neural networks (PINNs). Since traditional neural network models require large datasets and lack physical interpretability, physics-informed variants were used, to integrate physical laws into the training. The goal of this thesis is to use physics-informed neural networks to estimate patient-specific Windkessel parameters for six aortic branches, integrating pressure and flow data along with each model's differential equations, reaching biologically meaningful results in a non-invasive way. The validity of the proposed method was assessed against known biological constraints - specifically time decay constraints and net peripheral resistance - and further evaluated through waveform and frequency-domain plots.

2 Arterial Theoretical Background

2.1 General Anatomy of the Aorta

The aorta is the first arterial segment of the systemic blood circulation connected to the heart [1]. It is the largest artery and is responsible for transporting oxygenated blood to the rest of the human body. Other than its conduit function, it possesses a buffering function due to its compliance characteristic [2]. That way, the aorta is able to smooth pressure fluctuations as well as distribute blood to tissues, all while maintaining its structural integrity. According to [3], 85% of the aortic compliance comes from the thoracic aorta (the portion of the aorta that runs through the chest cavity).

The thoracic aorta can be divided into five key segments (Figure 1, by [4] found in Vascular Model Repository):

- RSA: Right Subclavian Artery
- RCCA: Right Common Carotid Artery

- LCCA: Left Common Carotid Artery
- LSA: Left Sublcavian Artery
- DAo: Descending Aorta

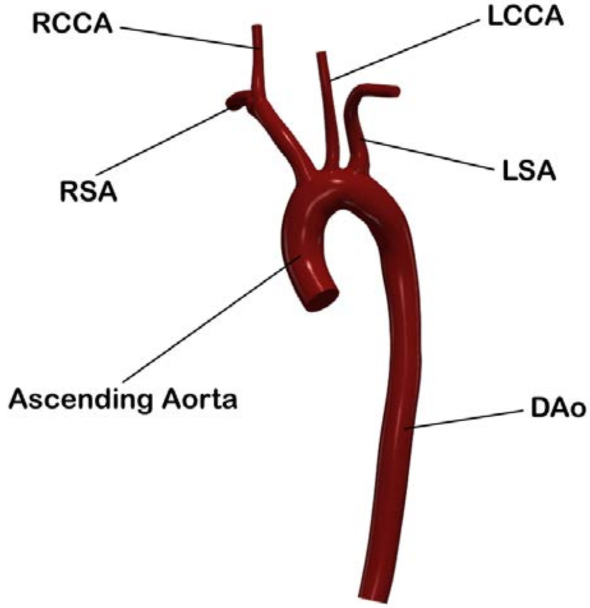

Figure 1: The aorta and its segments.

2.2 Aortic Dissection

The aorta, which is composed of intimal, medial and adventitial layers, is prone to mechanics-triggered injuries [1]. One of the most catastrophic and non-traumatic cardiovascular diseases, with very high mortality rate is aortic dissection.

There are two stages describing aortic dissection [5]:

1. Tear of the intima layer, after which, blood tracks through and separates it from the underlying media.

2. The single lumen of the aorta is divided into a true and a false lumen (TL - FL).

Aortic dissection can be described by two different types; type A and type B, depending on whether the ascending aorta is involved or not (Figure 2, modified figure by [6]). Type A, which involves the ascending aorta, needs prompt surgical treatment, while type B, sparing the ascending aorta, can be treated medically [7]. The main cause of death regarding aortic dissection is not the initial tear, but is related to further dissection with ultimate rupture and death due to hemorrhage or cardiac tamponade [8].

For the purpose of this thesis, aortic dissection type B was investigated. In this case, DAo is divided into DAoTL (true lumen) and DAoFL (false lumen), adding one more segment to the already five-part aorta; RSA, RCCA, LCCA, LSA, DAoTL, DAoFL.

Figure 2: Type A (left) and Type B (right) aortic dissection.

2.3 Arterial Modeling

Mathematical modeling is a powerful tool for non-invasive diagnostics, with each model varying in complexity and objectives [9]. Valuable information can be gained using simulations and analyses of blood flow and pressure dynamics.

Arterial models vary, ranging from simple Windkessel models [10], to complex representations, such as [11]. Zero dimensional or lumped-parameter models assume a uniform contribution of the fundamental variables, while higher dimensional models recognize the variation of these parameters in space, as shown in Figure 3 by [12].

There are no inherently ”good” or ”bad” models. In reality, a model should be evaluated based on its intended purpose [9]. In this thesis, the lumped-parameter Windkessel models will be used, from the simplest, 2-element, to the most complex 4-element.

2.4 The Windkessel Model

William Harvey in 1733 and later Otto Frank in 1899 [13] formulated and popularized the first Windkessel model. It was the first of the lumped-parameter models class where distributed properties of the arterial tree are lumped into a limited number of discrete components, neglecting their spatial distribution [14].

The Windkessel model provides us with a way to account for arterial blood pressure in terms of compliance of the large elastic arteries, and the resistance of the smaller arteries with an analogy of either a hydraulic system or an electrical circuit [15], as shown in Figure 4 by [16]. In the electrical circuit analogy, the blood flow Q(t) is modeled as the electrical current I(t), and the arterial pressure wave P(t) as a time-varying electrical potential V(t).

There are two-, three-, and four-element models, with each element resulting in better description of the relation between arterial pressure and flow [17]. It is important to note

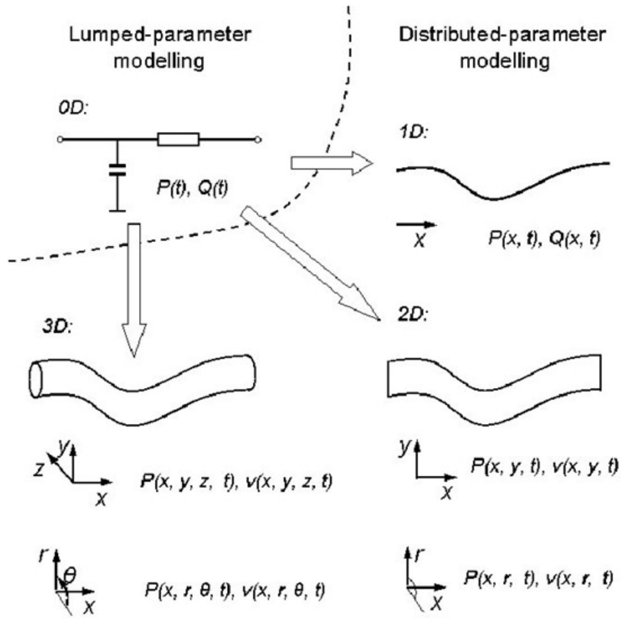

Figure 3: Different scales of modeling.

that adding more parameters, while drawing a better picture of the model, obscures their anatomical or physiological counterpart [18].

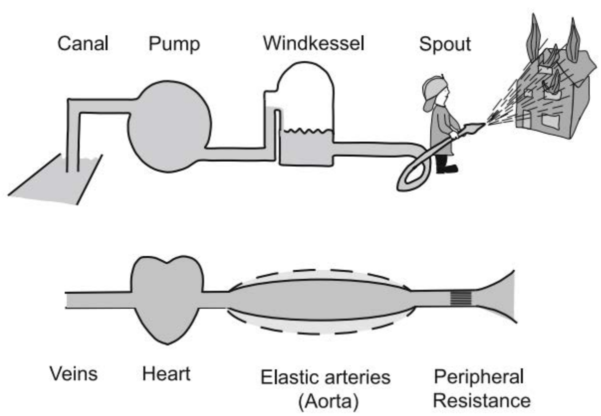

Figure 4: The concept of the Windkessel.

2.4.1 Two-Element Windkessel Model (W2)

As mentioned above, Otto Frank first derived the now know two-element Windkessel model in 1899. It is the simplest of the Windkessel family, but provides fundamental insight into the relationship between blood flow and pressure. Consisting of a resistance and a compliance element, the former is mainly found in the smallest arteries and arterioles, while the latter is mainly determined by the elasticity of the large conduit arteries [16], [19].

Its electrical analog is a parallel connection of a resistor (R) and a capacitor (C) [14], as shown in Figure 5.

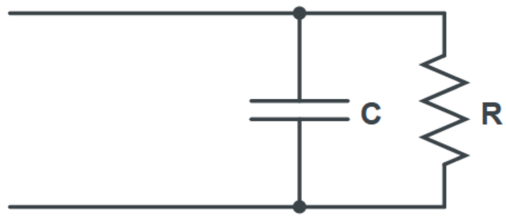

Figure 5: The two-element Windkessel model. Figure created in CircuitLab.

$$\left.\begin{array}{l}\dfrac{dV_C(t)}{dt} = \dfrac{I(t)}{C} - \dfrac{V_C(t)}{RC} \\ V(t) = V_C(t)\end{array}\right\} \quad \begin{array}{l}\dfrac{dP_C(t)}{dt} = \dfrac{Q(t)}{C} - \dfrac{P_C(t)}{RC} \\ P(t) = P_C(t)\end{array} \tag{1}$$

2.4.2 Three-element Windkessel Model (W3)

Progress in electromagnetic flow meters allowed for measurement of aortic flow, which showed that in systole, the relation between pressure and flow was poorly depicted by the two-element Windkessel [20]. Thankfully, the measurement of aortic flow, along with the development in computing capabilities, that allowed for Fourier analysis of pressure and flow waveforms, the calculation of input impedance became possible [21].

This possibility pointed out what the two-element Windkessel model was lacking. It was clear that for high frequencies the input impedance's modulus reduced to negligible values and its phase reached -90°, behavior, that according to [16], was contradictory to data derived in mammals, with the impedance modulus decreasing to a plateau value and the phase angle hovering around zero.

It was later found that the constant level of input impedance modulus at high frequencies was equal to the characteristic impedance of the proximal aorta [16], leading to the addition of characteristic impedance (Z) to the two-element Windkessel model, [22], in the form of a resistor because of its units and not of its physical meaning (Figure 6). The characteristic impedance is a link between the lumped Windkessel model and wave travel aspects of the arterial system, incorporating wave speed, blood density and aortic cross-sectional area [16].

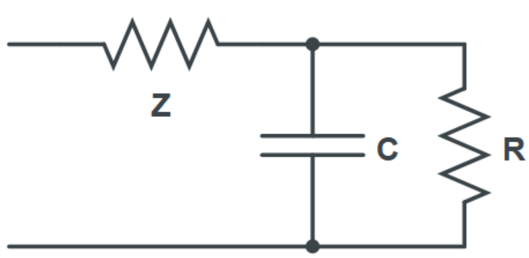

Figure 6: The three-element Windkessel model. Figure created in CircuitLab.

$$
\left.\begin{aligned}
\frac{dV_C(t)}{dt} &= \frac{I(t)}{C} - \frac{V_C(t)}{RC} \\
V(t) &= V_C(t) + ZI(t)
\end{aligned}\right\} \quad
\begin{aligned}
\frac{dP_C(t)}{dt} &= \frac{Q(t)}{C} - \frac{P_C(t)}{RC} \\
P(t) &= P_C(t) + ZQ(t)
\end{aligned}
\tag{2}
$$

2.4.3 Four-element Windkessel Model (W4)

There are some areas, especially in low frequencies of the input impedance, where the three-element Windkessel is inaccurate [16]. For this reason, an inertial term in parallel with the characteristic impedance was introduced (W4P, Figure 7) as an inductor (L), better predicting ascending aortic pressure from aortic flow [23].

The inertance term can also be put in series with the characteristic impedance (W4S, Figure 8), sometimes fitting data better than the W4P, but suffering from the assumption that the characteristic impedance Zc is a part of total peripheral resistance [24]. [25] also showed that for estimating the model's parameters, W4S was closer to calculated values and yielded a better fit compared to W4P, which yielded unrealistic estimations due to model mismatch.

Generally, inertance is very difficult to estimate, raising an argument to prefer the three-element Windkessel model in many applications [16], [26].

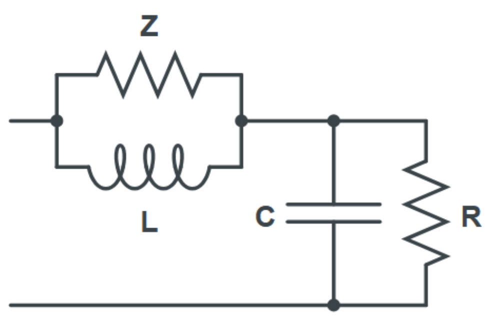

Figure 7: The four-element Windkessel model, L-Z parallel. Figure created in CircuitLab.

$$
\left.\begin{aligned}
\frac{dI_L(t)}{dt} &= \frac{Z(I(t) - I_L(t))}{L} \\
\frac{dV_C(t)}{dt} &= \frac{I(t) - \frac{V_C(t)}{R}}{C} \\
V(t) &= V_C(t) + Z(I(t) - I_L(t))
\end{aligned}\right\} \quad
\begin{aligned}
\frac{dQ_L(t)}{dt} &= \frac{(Q(t) - Q_L(t))}{L} \\
\frac{dP_C(t)}{dt} &= \frac{Q(t) - \frac{P_C(t)}{R}}{C} \\
P(t) &= P_C(t) + Z(Q(t) - Q_L(t))
\end{aligned}
\tag{3}
$$

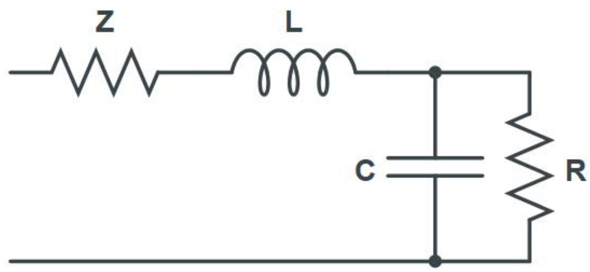

Figure 8: The four-element Windkessel model, L-Z in series. Figure created in CircuitLab

$$\left.\begin{aligned} \frac{dI_L(t)}{dt} &= \frac{V(t)-(V_C(t)-RI_L(t))}{L} \\ \frac{dV_C(t)}{dt} &= \frac{I_L(t)-(V_C(t)/R)}{C} \\ V(t) &= V_C(t)+ZI(t)+L\frac{dI(t)}{dt} \end{aligned}\right\} \quad \begin{aligned} \frac{dQ_L(t)}{dt} &= \frac{P(t)-(P_C(t)-RQ_L(t))}{L} \\ \frac{dP_C(t)}{dt} &= \frac{Q_L(t)-(P_C(t)/R)}{C} \\ P(t) &= P_C(t)+ZQ(t)+L\frac{dQ(t)}{dt} \end{aligned} \tag{4}$$

Equations (1)-(4) are derived from Kirchoff's laws of voltage and current, applied on the electrical circuits of Figures 5–8.

Table 1 by [16] summarizes the differences between the two-, three- and four-element Windkessel models.

	Two-element Windkessel	Three-element Windkessel	Four-element Windkessel
P_{diast}	RC-time	RC-time	RC-time
Total waveshape	Poor	Good	Good
Impedance	Poor at high freq.	Small error at high freq.	Good at all freq.
Compliance estimate	Good	Overestimation	Accurate estimation
Inertance	NA	NA	Difficult to estimate
$P_{mean}/flow_{mean}$	Resistance	Resistance + Characteristic imp.	Resistance

Table 1: Comparison of the different-element Windkessel models.

3 Computational Methods

3.1 Neural Networks

A neural network (NN) is an interconnected assembly of simple processing units called neurons, (Figure 9, by [27]), that communicate and transmit information. The processing ability of the network is stored in the inter-unit connection weights, obtained by a process of learning from a set of training patterns [27]. The goal of the neural network is to ultimately minimize an error, expressed as the loss function. Defining a suitable loss function with respect to a dataset, gives way to training, which is the determination of the weight values [28].

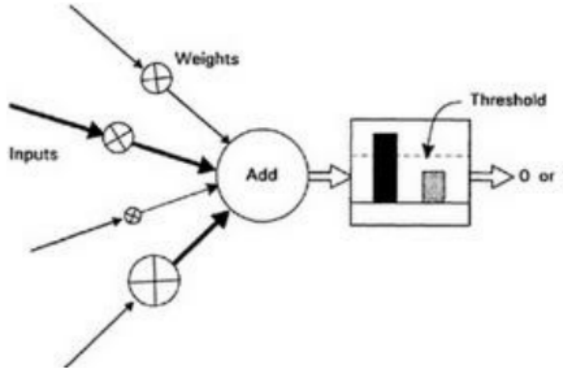

Figure 9: A neuron, receiving multiple inputs with different weights, and producing an output.

A typical neural network consists of three main types of layers: an input layer receiving the external data, one or more hidden layers where intermediate computations take place and an output layer producing the final prediction (Figure 10, by [29]).

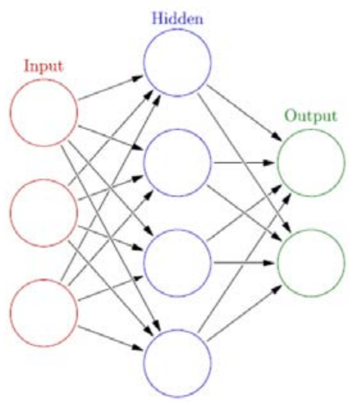

Figure 10: A typical neural network.

During training, a neural network operates in iterative cycles:

1. Forward pass: Inputs are passed through the network layer by layer to compute the predicted output.

2. Loss computation: The predicted output is compared to the true value using a loss function, which quantifies the error.

3. Backpropagation: The error is propagated backward through the network to compute gradients of the loss with respect to each weight.

4. Weight update: The weights are adjusted using an optimization algorithm (typically gradient descend) to reduce the loss in future iterations.

Through this process, the network gradually ”learns” the patterns in the data and improves its predictions.

3.2 Limitations of Traditional Neural Networks

Generally, traditional neural networks have remarkable performance in image recognition, or natural language processing topics. When it comes to scientific and physics-based problems, NNs show important limitations.

The fact that they require large volumes of high-quality data, poses a huge problem for real applications where measurements may be scarce, expensive or impossible to obtain. Also, being purely data-driven translates to lack of physical insight. All in all, regarding complex physical problems, traditional NNs show poor generalization performance, which limits their reliability.

3.3 Physics-Informed Neural Networks

Physics-Informed Neural Networks (PINNs) pose a new class of universal function approximators capable of encoding any underlying physical laws that govern a given data-set and can be described by partial differential equations [30]. Merging deep learning with the powerful capacity of mathematical physics, they can produce accurate and physically consistent predictions even when data is noisy or imperfect. This way, deep learning could be a mesh-free approach by taking advantage of automatic differentiation (one forward pass to compute the values of all variables, and one backward to compute the derivatives) [31]. Ill posed and inverse problems can also be solved as easily as forward problems, estimating unknown parameters from limited observations.

Regarding the cardiovascular system, [15] proposed that the loss function is typically composed of multiple terms (Figure 11):

- A residual loss, which enforces the satisfaction of the governing differential equations.
- An interface loss, which imposes continuity or boundary conditions at interfaces or domain boundaries.
- A measurement loss, which minimizes the discrepancy between the network's predictions and observed data.

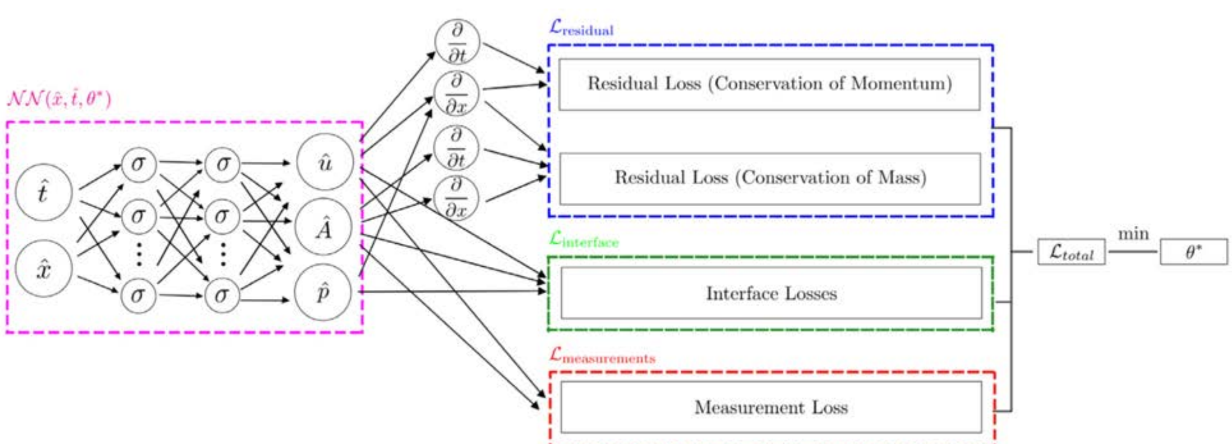

Figure 11: The PINN algorithm.

3.3.1 Software

Since Python is the most dominant programming language for machine learning, it was selected to implement the PINN framework. There are numerous libraries designed for Machine Learning (ML) such as TensorFlow, PyTorch, Keras and JAX, that all use automatic differentiation for solving differential equations. There are others though specifically created for physics-informed ML, and one in particular, that was the primary tool for this thesis, is the library DeepXDE.

MATLAB was also used for the creation of Bode plots, as well as input impedance plots, showing the system's behavior in the frequency domain, with the estimated parameters for each model.

3.3.2 DeepXDE Library

DeepXDE is a flexible Python library, designed for deep learning applications. It is able to solve forward problems as well as inverse ones and its main advantage is its simplicity. After defining the geometry, the governing equations, the initial/boundary conditions, the data and the network architecture, DeepXDE binds them together and the PINN is ready for training, as shown in Figure 12 by [31]. Also, the addition of callbacks enables the user to monitor the training process of the neural network, or make modifications in real time, e.g., stopping early in case of overfitting or changing the learning rate after a number of iterations [31].

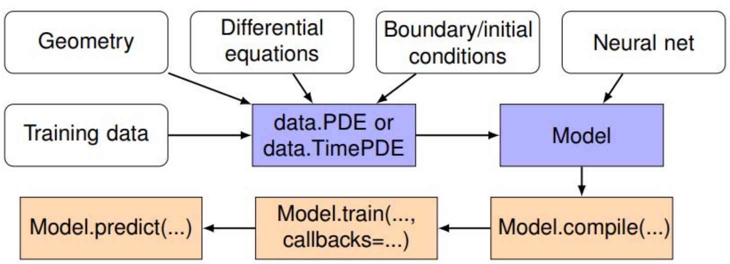

Figure 12: The DeepXDE Flowchart.

4 Methods

4.1 The Inverse Problem

The method tested in this thesis requires the solution of four inverse problems, one for each Windkessel model. The goal is to use the differential equations of each model and estimate its parameters. Implementing the differential equations in the DeepXDE framework requires some minor modifications in order to have a clear residual loss for the program to track and minimize. For each model, the inserted equations have the following form:

- W2: (1) $\rightarrow$

$$\frac{dP(t)}{dt} - \frac{Q(t)}{C} + \frac{P(t)}{RC} = residual \tag{5}$$

- W3: (2) $\rightarrow$

$$C\frac{dP(t)}{dt} + \frac{P(t)}{R} - CR\frac{dQ(t)}{dt} - \left(1 + \frac{Z}{R}\right)Q(t) = residual \tag{6}$$

- W4P: (3) $\rightarrow$

$$\begin{aligned} L\frac{dQ_L(t)}{dt} - Z(Q(t) - Q_L(t)) &= residual(a) \\ C\frac{dP_C(t)}{dt} - Q(t) + \frac{P_C(t)}{R} &= residual(b) \\ P(t) - P_C(t) - Z(Q(t) - Q_L(t)) &= residual(c) \end{aligned} \tag{7}$$

- W4S: (4) $\rightarrow$

$$\begin{aligned} \frac{dP_C(t)}{dt} + \frac{P_C(t)}{RC} - \frac{Q(t)}{C} &= residual(a) \\ P(t) - P_C(t) - ZQ(t) - L\frac{dQ(t)}{dt} &= residual(b) \end{aligned} \tag{8}$$

4.2 Data Acquisition

In order to estimate each model's parameters for all six arteries using the PINN method, pressure and flow data are required fo each branch of the aorta. [32] kindly provided this data (Figure 13), with pressure obtained by a 1D simulation in the Nektar1D solver and flow by clinical in-vivo measurements from Queen Elizabeth University Hospital, interpolated to match the number of data points of the simulated pressure. The difference in the origins of the data will create issues that will be discussed in later Sections.

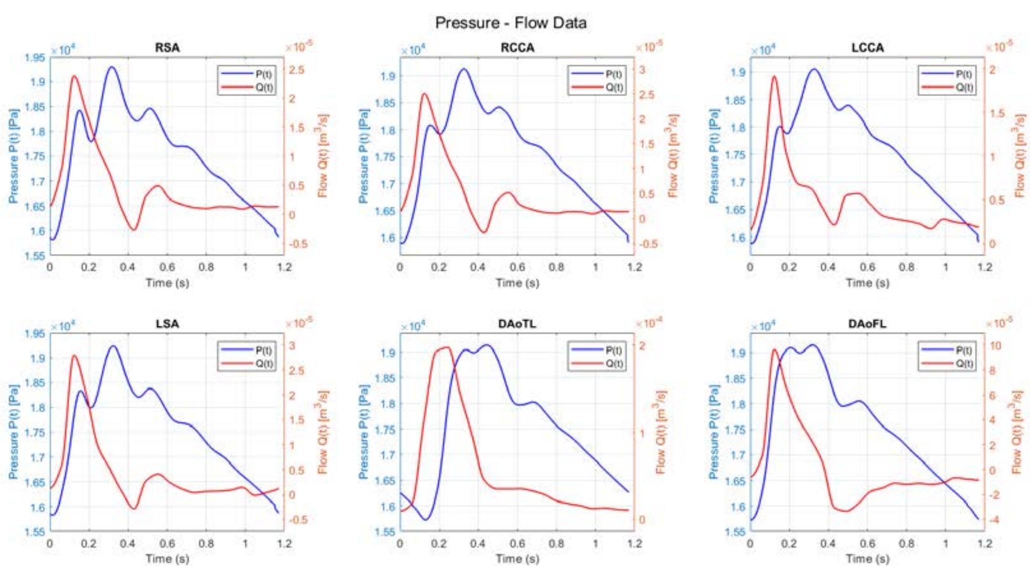

Figure 13: Pressure and Flow data.

4.3 Windkessel Parameters' Initialization

Before training, initial values for the trainable parameters are required. Utilizing the proposed equations by [33],[34] and [25]:

- Characteristic impedance:

$$Z = \frac{\rho c_{pwv}}{A_0} \tag{9}$$

- Peripheral resistance:

$$R = Z(\frac{\lambda}{2\phi^4 - \lambda}) \tag{10}$$

- Arterial compliance:

$$C = C_0(\frac{2\lambda\phi^3}{1 - 2\lambda\phi^3}), C_0 = \frac{A_0 l}{\rho(c_{pwv})^2} \tag{11}$$

- Inertance:

$$L = \frac{\rho l}{A_0} \tag{12}$$

Where, $\lambda = 0.68$, $\phi = \sqrt{0.6}$, are chosen scaling factors, $c_{pwv} = 4.38ms^{-1}$ is the 4D flow-MRI derived arterial pulse wave velocity in the thoracic aorta, $\rho = 1,060kgm^{-3}$ is the blood density, A_0 is the average branch vessel cross sectional area and l is the branch vessel length. All values where obtained by [32].

Branch	Branch length (m $\times 10^{-1}$)	Mean cross sectional area (m^2 $\times$ 10^{-5})
RSA	1.10	4.04
RCCA	0.46	1.34
LCCA	0.80	3.35
LSA	1.48	3.05
DAoTL	1.87	12.50
DAoFL	1.85	25.70

Table 2: Branch length - Mean cross sectional area for each artery.

The resulting initial values are shown in Table 3.

Branch	R ($\times 10^9$)$[Pasm^{-3}]$	C ($\times 10^{-10}$)$[m^3Pa^{-1}]$	Z ($\times 10^7$)$[Pasm^{-3}]$	L ($\times 10^6$)$[Pas^2m^{-3}]$
RSA	1.95	3.75	11.50	2.89
RCCA	5.89	0.52	34.6	3.64
LCCA	2.36	2.26	13.90	2.53
LSA	2.59	3.81	15.2	5.14
DAoTL	0.63	19.7	3.71	1.59
DAoFL	0.31	40.20	1.81	0.76

Table 3: Initial values.

It was later found that setting all the initial values as 1.00 with each parameter's corresponding order of magnitude, assisted in the training process and the parameters' convrergence. For this reason, and for generalization purposes, all initial values were set to 1.00, and so the calculations above determined just the order of magnitude for each component (except for arterial compliance where $\times 10^{-9}$ produced more biologically consistent results that will be discussed later on).

4.4 PINN Structure

As mentioned in Section 3.3.2, the application is as easy as simply defining all the aspects of the problem.

Firstly, since the equations' residuals are being used, and because the algorithm itself cannot distinguish the quality of an error just its quantity, every term inside each equation has to be of similar order of magnitude, around $\mathcal{O}(10^0)$, while keeping unit and dimensional consistency. For this reason:

- Pressure and flow data were normalized using Min-Max normalization [35]:

$$X_{new} = \frac{X - X_{min}}{X_{max} - X_{min}}$$

- The parameters were scaled down, just inside the equations, divided by constant values, each with the same order of magnitude as the corresponding parameter:

$$R_{eq} = \frac{R}{R_0}, \;\; C_{eq} = \frac{C}{C_0}, \;\; Z_{eq} = \frac{Z}{Z_0}, \;\; L_{eq} = \frac{L}{L_0}$$

  where $R_0 = 10^9 Pasm^{-3}$, $C_0 = 10^{-9} m^3 Pa^{-1}$, $Z_0 = 10^7 Pasm^{-3}$, $L_0 = 10^6 Pas^2 m^{-3}$

This way, both pressure and flow data along with the parameters, regarding the equations' residuals, became dimensionless and of similar order of magnitude.

Another important step pre-training, was to define each parameter as a logarithm, in order to keep positive and non-exploding values during training. As a result, the exponentials of the parameters where used in the equations, and post-training, to extract the actual values.

Callbacks of the class `ParameterTracker` where set in order to obtain each parameter's value every 1000 iterations for future plotting and understanding its behavior. The residuals for each artery talked about in Section 4.1, where combined into one function called `combined_equations`, along with one more equation regarding the net peripheral resistance (R_T), where:

$$R_T = \frac{P_{Mean}}{\bar{Q}_{in}}, \;\; P_{Mean} = P_{Dia} + \frac{1}{3}(P_{Sys} - P_{Dia}) \tag{13}$$

from [36], and according to Table 1, the following residuals can be obtained:

- W2, W4P:

$$\frac{1}{R_T} - \sum_{j=1}^{n} \frac{1}{R_j} = residual \tag{14}$$

- W3, W4S:

$$\frac{1}{R_T} - \sum_{j=1}^{n} \frac{1}{R_j + Z_j} = residual \tag{15}$$

where n is the number of arterial branches. The data required to estimate the net peripheral resistance (R_T) was also provided by [32].

Regarding the geometry of the problem, it was set as a time domain from 0 to 1.17 seconds, lasting roughly one cardiac cycle, using the function `deepxde.geometry.TimeDomain` and the data acquired by [32] were assigned to each output of the neural network using the `deepxde.icbc.PointSetBc` function. For W4S and W4P, initial conditions were also needed since for the former, P_C , and for the latter both P_C and Q_l had to be estimated, using `deepxde.IC`. The initial conditions that were applied were the first values from the pressure and flow dataset respectively.

Using `deepxde.data.PDE`, all the above where combined into a single variable called `data` - while also setting the number of collocation points inside the domain to 100 (`num_domain = 100`) - ready to be passed through the neural network and start the training process.

The fully connected neural networks' architectures that were used for this purpose were mainly the same for all models, with the only differences being in the output layer. W2 and W3 share no differences, consisting of 1 neuron in the input layer representing the temporal dimension, 3 hidden layers with 128 neurons each and 12 neurons in the output layer (Figure 14), predicting pressure and flow data for each of the six arteries. Regarding W4, more neurons in the output are needed, since W4S requires the estimation of P_C before estimating P and Q, and W4P the estimation of both P_C and Q_l. For this reason, they have 18 and 24 neurons in the output layer respectively (Figures 15,16). The architectures mentioned were chosen based on the complexity of the problem as well as the computational resources available.

After defining the network architectures, the `deepxde.Model` function was used to combine the `data` and `net` for each Windkessel, and form the complete physics-informed neural networks (Figures 17–20).

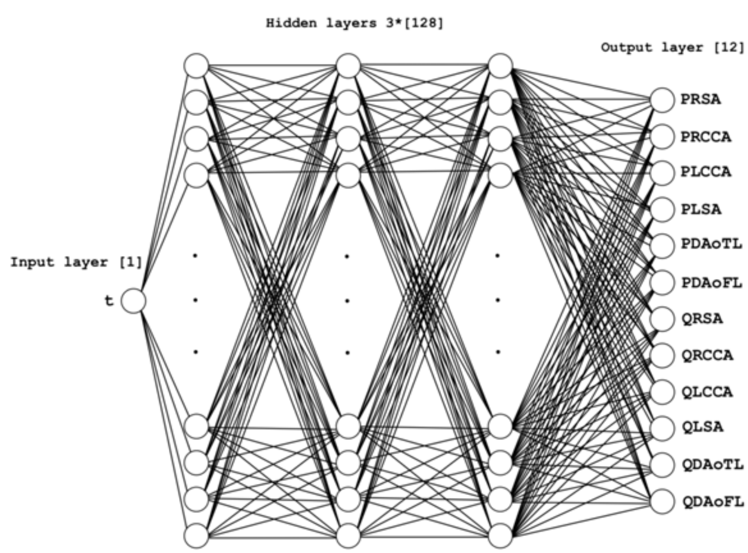

Figure 14: NN Architecture for W2 and W3.

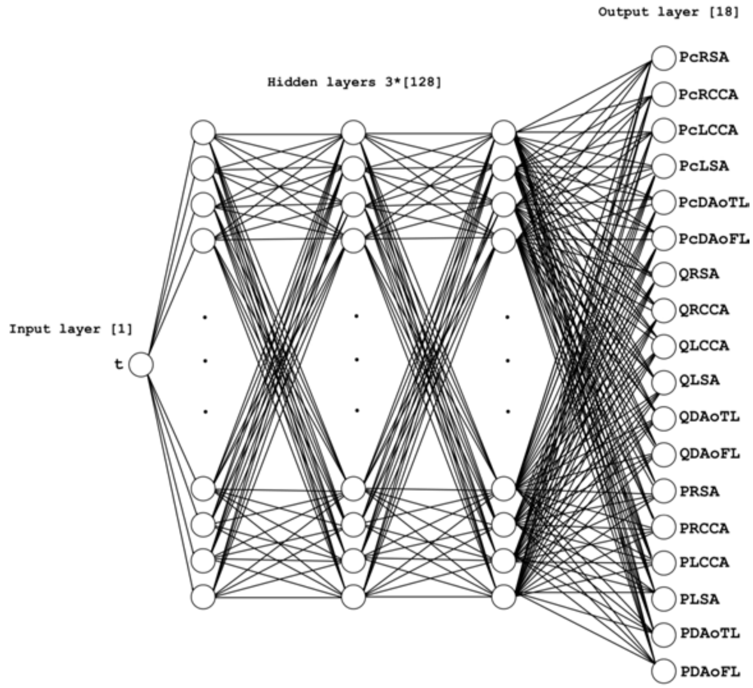

Figure 15: NN Architecture for W4S.

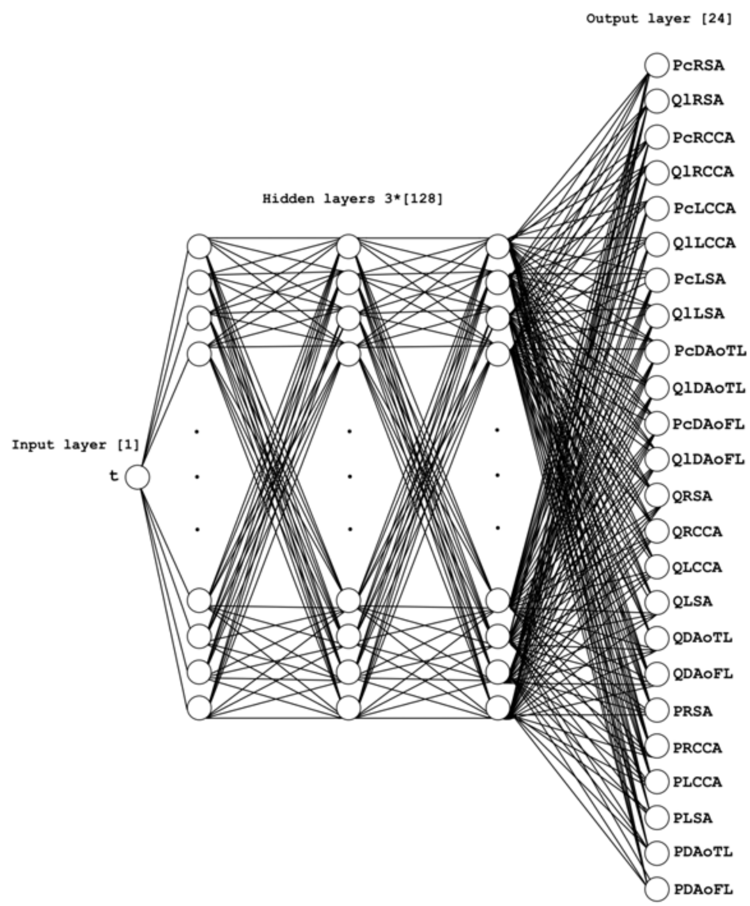

Figure 16: NN Architecture for W4P.

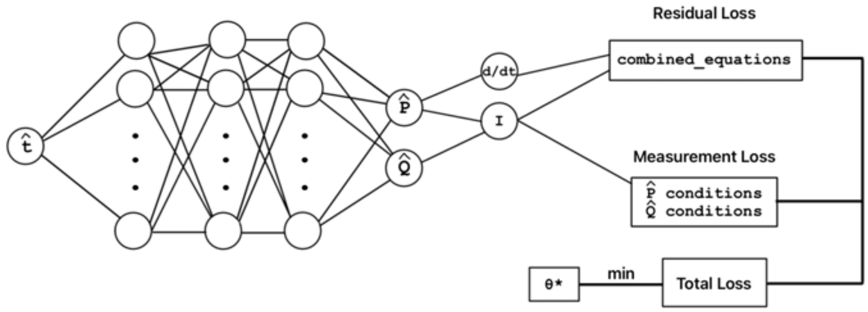

Figure 17: PINN architecture for W2.

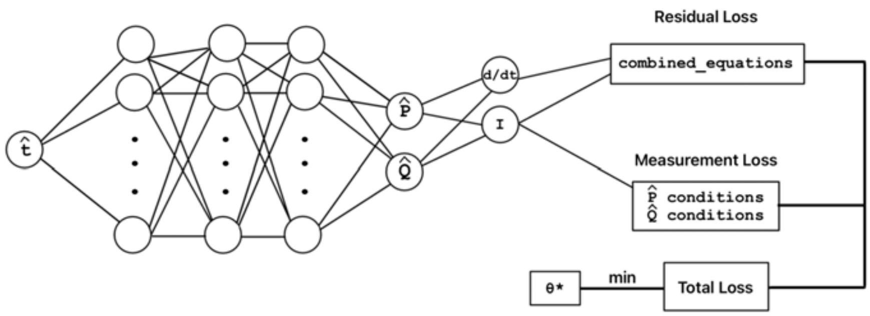

Figure 18: PINN architecture for W3.

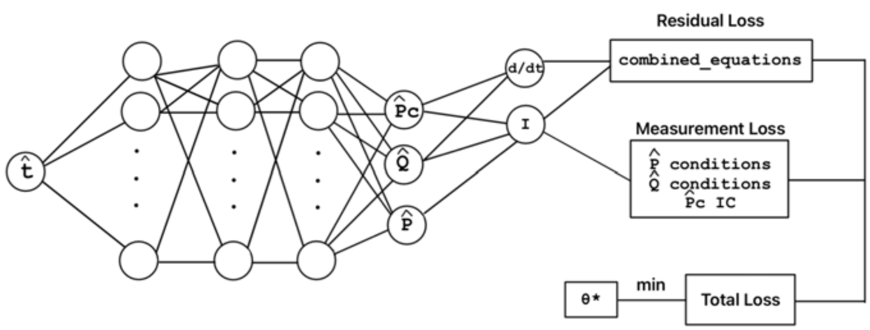

Figure 19: PINN architecture for W4S.

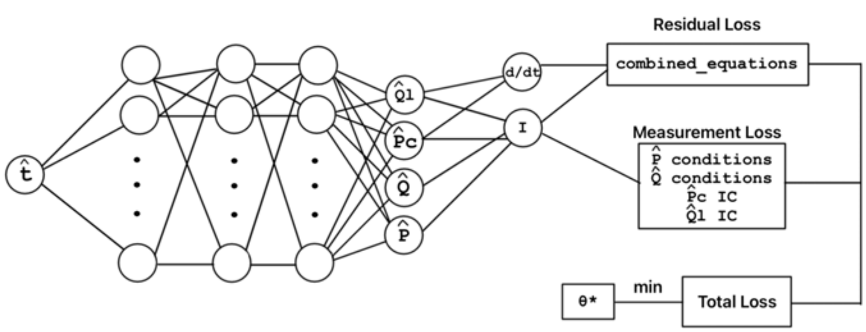

Figure 20: PINN architecture for W4P.

Compiling the model was done using the `model.compile` function, while also setting the optimizer `"Adam"`, the initializer `"Glorot uniform"` and the learning rate at 0.001. The initial weights for each component of the loss function began at 1, but after trial and error trying to achieve both parameter convergence and acceptable data fitting, it was observed that the measurement loss generally required bigger weights than the rest of the components, varying across the different models. The best produced results for each model where at 15^3 iterations for W2, 20^3 iterations for W3 and W4S, and 40^3 iterations for W4P.

5 Results

5.1 Calibrated Windkessel Parameters

After training, using the callback mentioned in Section 4.4, the parameters' values every 1000 iterations were extracted, in order to plot their behavior and ensure that convergence was reached (Figures 21–24).

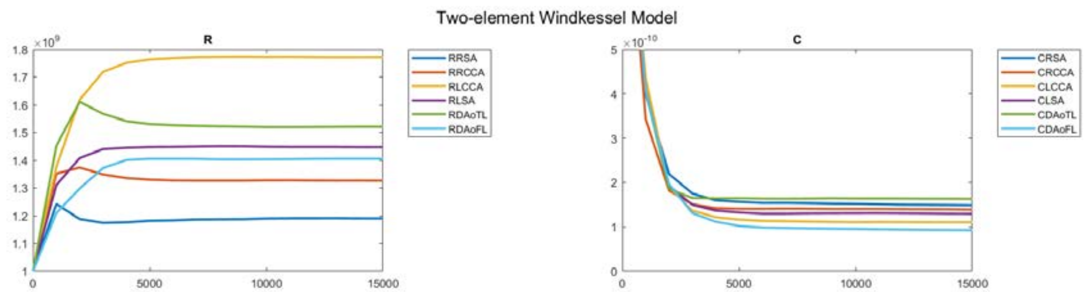

Figure 21: Parameter Convergence for W2.

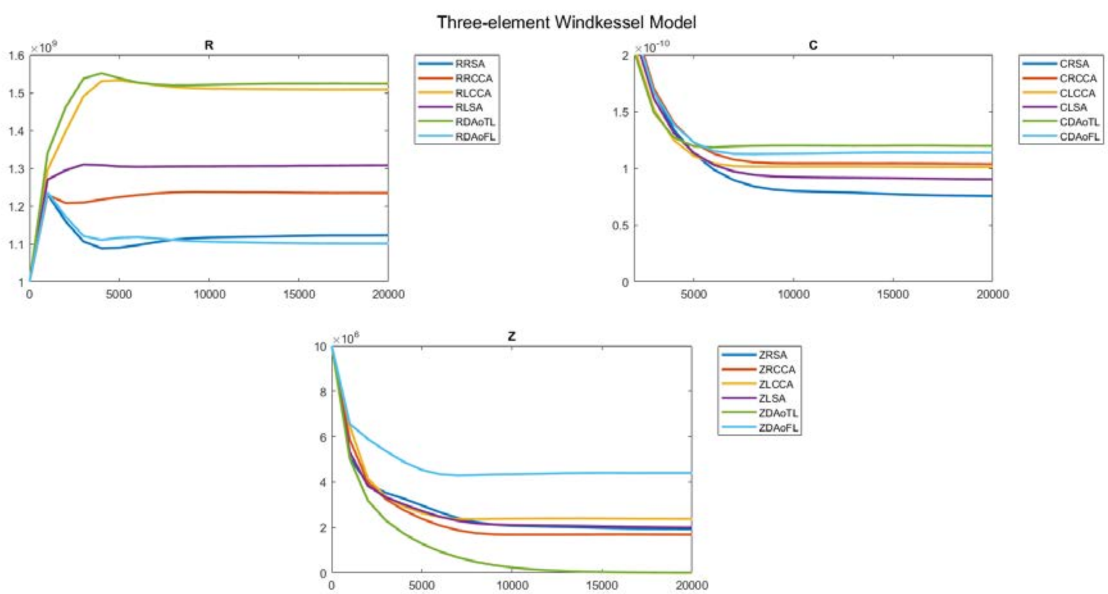

Figure 22: Parameter Convergence for W3.

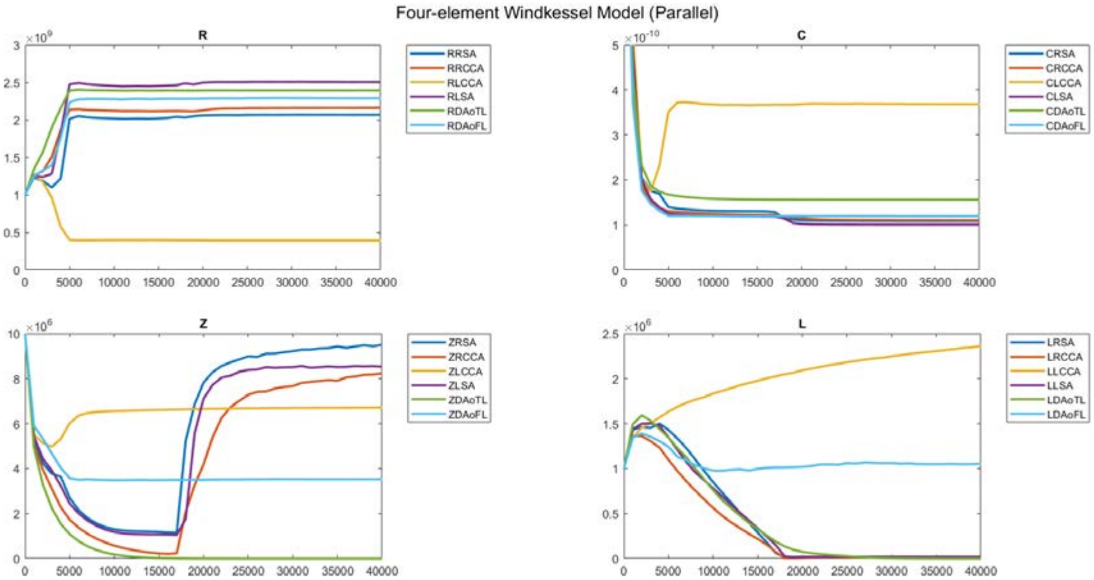

Figure 23: Parameter Convergence for W4P.

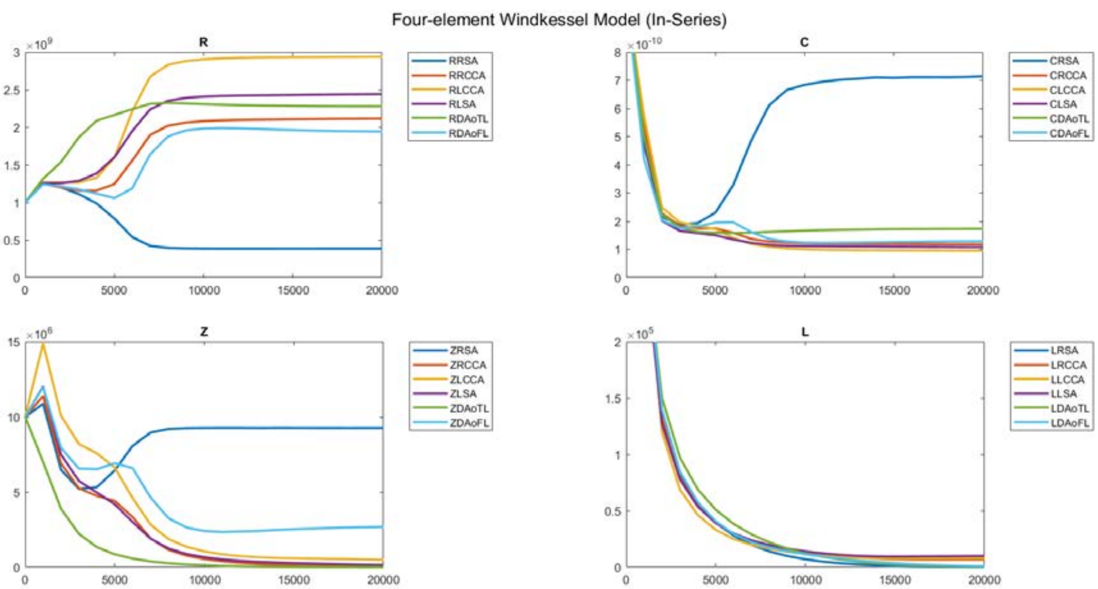

Figure 24: Parameter Convergence for W4S.

Generally, W2 and W3's convergences were reached easily, since the underlying equations were straightforward and easily applicable. Regarding W4 and especially W4P, due to the necessary initialization and estimation of P_C and Q_l, the problem was more challenging, and could potentially be defined more accurately for better results.

The final parameter values (taking into consideration both residual loss and data fitting) are shown in Tables 4–7.

In order to test whether the final values listed have biological meaning, it was first ensured that equations 14, 15 were satisfied. Regarding W2, the resulting sum has an error of 11.3% , W3 dropped to 1.68% and for W4P, W4S the calculated error was 0.21% and 1.13% respectively (Table 8).

Branch	R ($\times10^9$)[Pasm^{-3}]	C ($\times10^{-10}$)[m$^3Pa^{-1}$]
RSA	1.19	1.49
RCCA	1.33	1.39
LCCA	1.77	1.1
LSA	1.45	1.3
DAoTL	1.52	1.63
DAoFL	1.41	0.924

Table 4: W2 Parameter Values.

Branch	R ($\times10^9$)[Pasm^{-3}]	C ($\times10^{-10}$)[m$^3Pa^{-1}$]	Z ($\times10^7$)[Pasm^{-3}]
RSA	1.12	0.757	0.193
RCCA	1.23	1.04	0.168
LCCA	1.51	1.01	0.238
LSA	1.31	0.903	0.200
DAoTL	1.52	1.20	0.0004
DAoFL	1.10	1.14	0.440

Table 5: W3 Parameter Values.

Branch	R ($\times10^9$)[Pasm^{-3}]	C ($\times10^{-10}$)[m$^3Pa^{-1}$]	Z ($\times10^7$)[Pasm^{-3}]	L ($\times10^6$)[Pas$^2m^{-3}$]
RSA	2.07	1.08	0.951	0.021
RCCA	2.16	1.10	0.823	0.015
LCCA	0.392	3.68	0.671	2.36
LSA	2.50	1.01	0.853	0.02
DAoTL	2.39	1.56	$1.8 * 10^{-7}$	0.00045
DAoFL	2.29	1.20	0.353	1.05

Table 6: W4P Parameter Values.

Branch	R ($\times10^9$)[Pasm^{-3}]	C ($\times10^{-10}$)[m$^3Pa^{-1}$]	Z ($\times10^7$)[Pasm^{-3}]	L ($\times10^6$)[Pas$^2m^{-3}$]
RSA	0.386	7.14	0.926	0.0001
RCCA	2.11	1.18	0.002	0.007
LCCA	2.94	0.954	0.048	0.008
LSA	2.44	1.08	0.014	0.01
DAoTL	2.28	1.73	0.0003	0.0003
DAoFL	1.94	1.29	0.268	0.0008

Table 7: W4S Parameter Values.

	W2	W3	W4P	W4S	Measurement
Branch	$\frac{1}{R_j}(\times 10^{-10})$	$\frac{1}{R_j+Z_j}(\times 10^{-10})$	$\frac{1}{R_j}(\times 10^{-10})$	$\frac{1}{R_j+Z_j}(\times 10^{-10})$	$\frac{1}{R_T}(\times 10^{-10})$
RSA	8.40	8.89	4.84	25.3	
RCCA	7.54	8.09	4.63	4.73	
LCCA	5.64	6.62	25.5	3.40	
LSA	6.91	7.64	3.99	4.10	
DAoTL	6.57	6.56	4.18	4.39	
DAoFL	7.11	9.05	4.37	5.14	
$\sum$	42.20	46.80	47.50	47.06	47.60

Table 8: Net peripheral resistance constraint.

	W2	W3	W4P	W4S	Measurement
Branch	$RC(sec)$	$RC(sec)$	$RC(sec)$	$RC(sec)$	$\tau(sec)$
RSA	0.18	0.08	0.22	0.28	0.22
RCCA	0.18	0.13	0.24	0.25	0.21
LCCA	0.20	0.15	0.14	0.28	0.22
LSA	0.19	0.12	0.25	0.26	0.21
DAoTL	0.25	0.18	0.37	0.39	0.23
DAoFL	0.13	0.13	0.27	0.25	0.14

Table 9: Time decay constraint.

The peripheral resistance along with the arterial compliance must also satisfy the time decay equation from Table 1. More specifically, for every model, the product of R and C must be equal to the time decay in diastole. Using the pressure and flow waveforms to determine the diastole phase, the time decay τ was calculated for every arterial branch, via numerical integration, as the area formed under the pressure function $P(t) = P_0 e^{\frac{-t}{\tau}}$, [16], divided by $(P_1 - P_2)$ (selected pressure points), [21]. The results are shown in Table 9.

Due to this constrain, as mentioned in Section 4.3, the initial order of magnitude of the arterial compliance was set to $\times 10^{-9}$, instead of $\times 10^{-10}$.

5.2 Predicted Waveforms

After concluding that the calibrated parameters have, up to an acceptable point, biological meaning, they were used along with the trained PINN to reproduce pressure and flow waveforms, aiming to match the initial training data. The results are shown in Figures 25–32. It is clear that the two-element Windkessel model cannot estimate pressure and flow data with precision, but only capture the general shape, something that was expected (Section 2.4.2). The three-element Windkessel model predicts the initial waveforms almost perfectly, having only small deviations where the slope changes drastically. This has to do with the size of the neural network, and as will be shown later, even the four-element models struggle to capture this behavior (since the neural netowk has the same complexity). Regarding the more complex four-element Windkessel models, even though they also yield very accurate predictions, their increased computational burden limits their suitability as the preferred models.

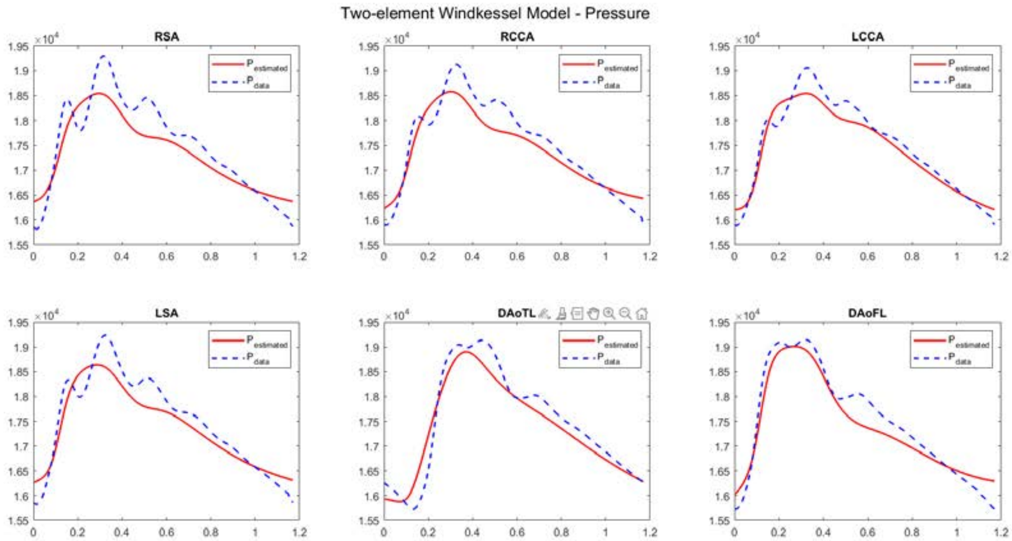

Figure 25: Predicted Pressure for W2.

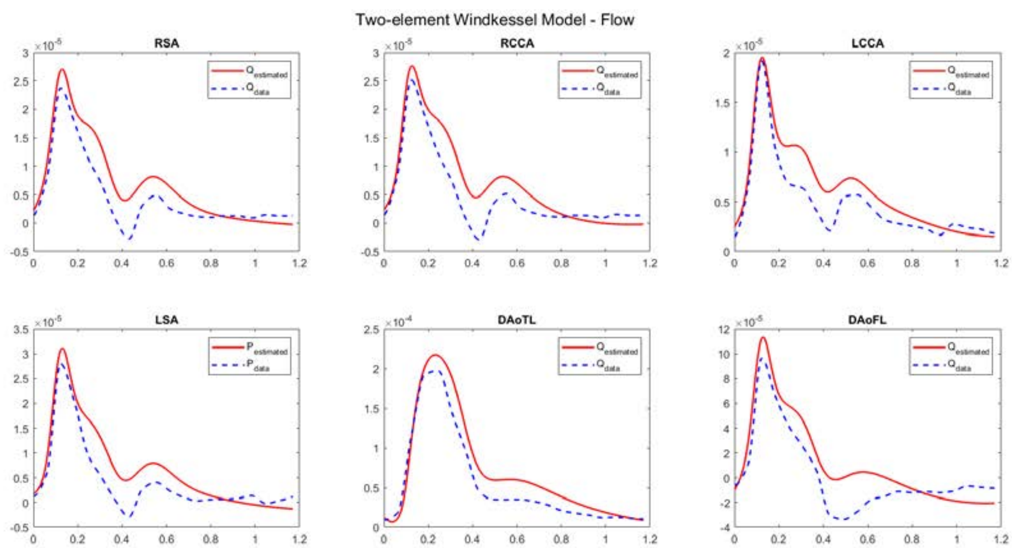

Figure 26: Predicted Flow for W2.

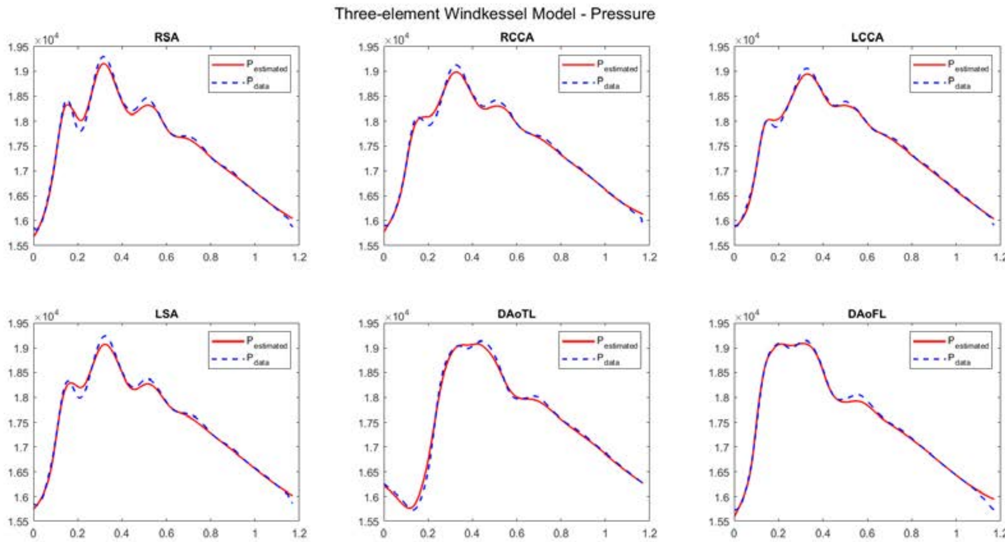

Figure 27: Predicted Pressure for W3.

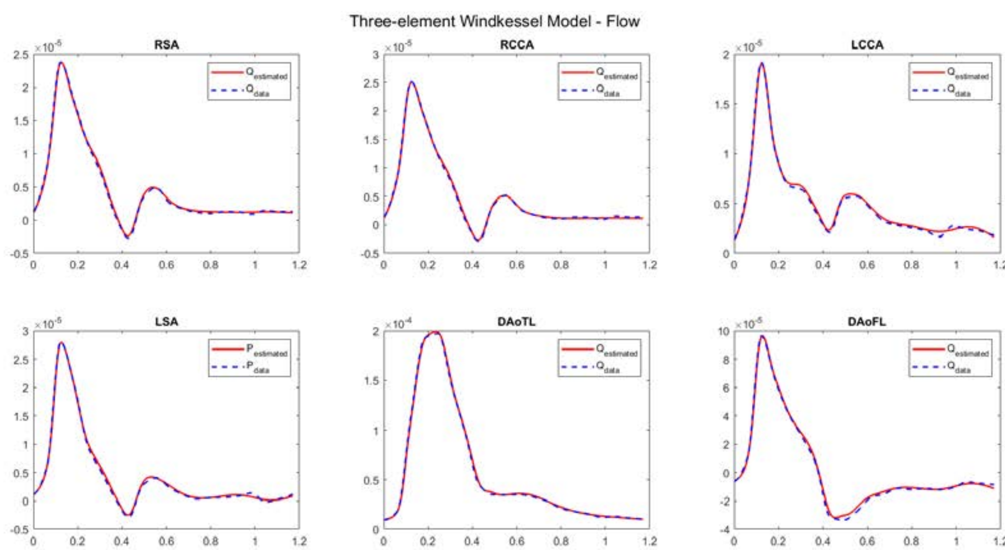

Figure 28: Predicted Flow for W3.

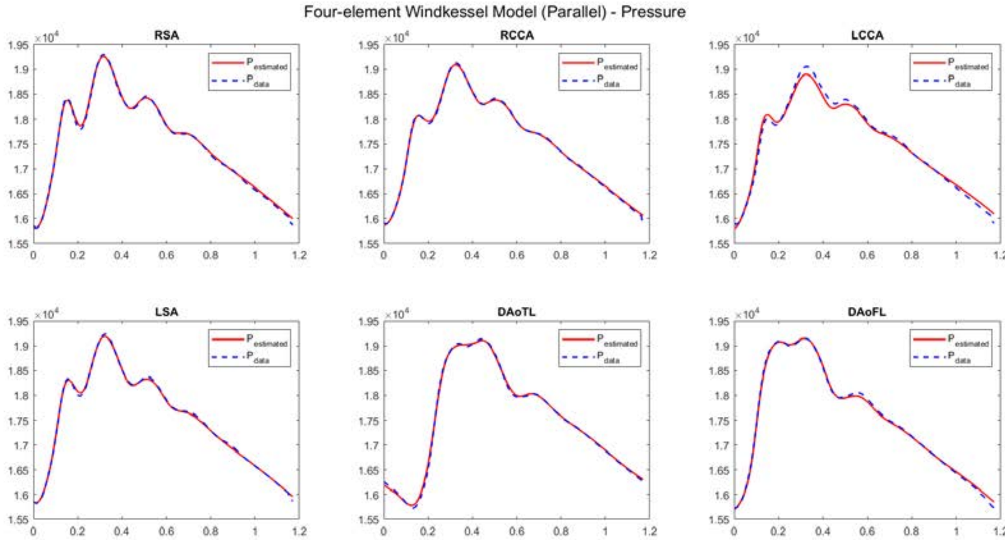

Figure 29: Predicted Pressure for W4P.

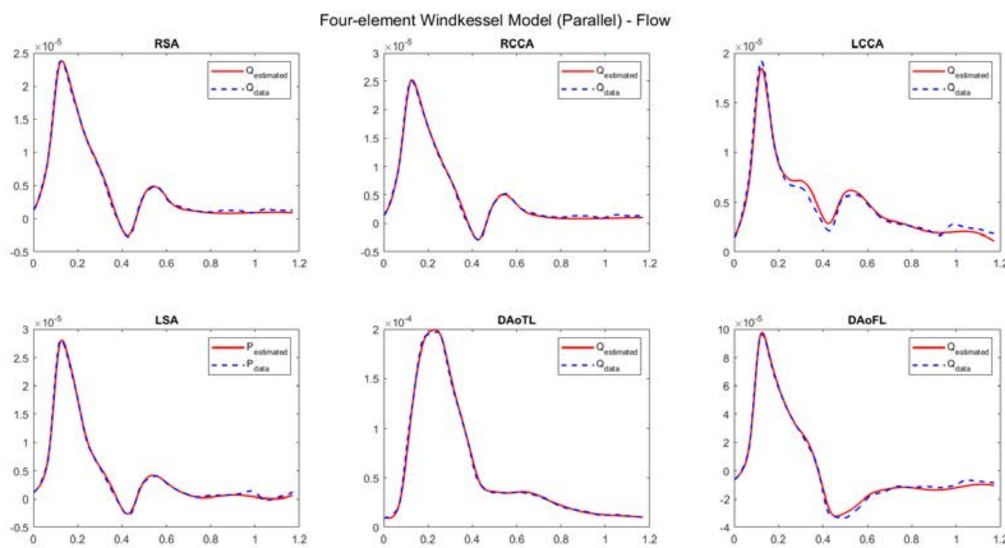

Figure 30: Predicted Flow for W4P.

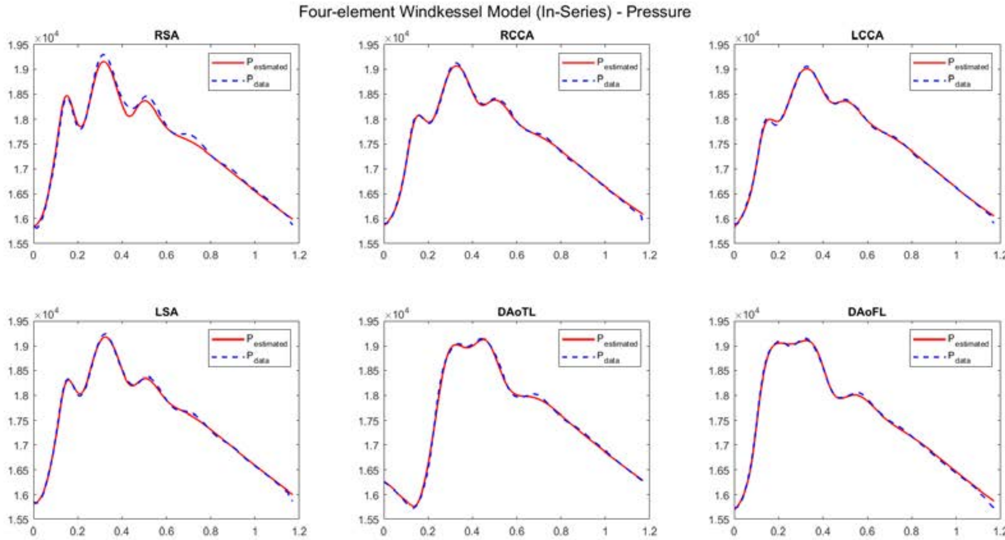

Figure 31: Predicted Pressure for W4S.

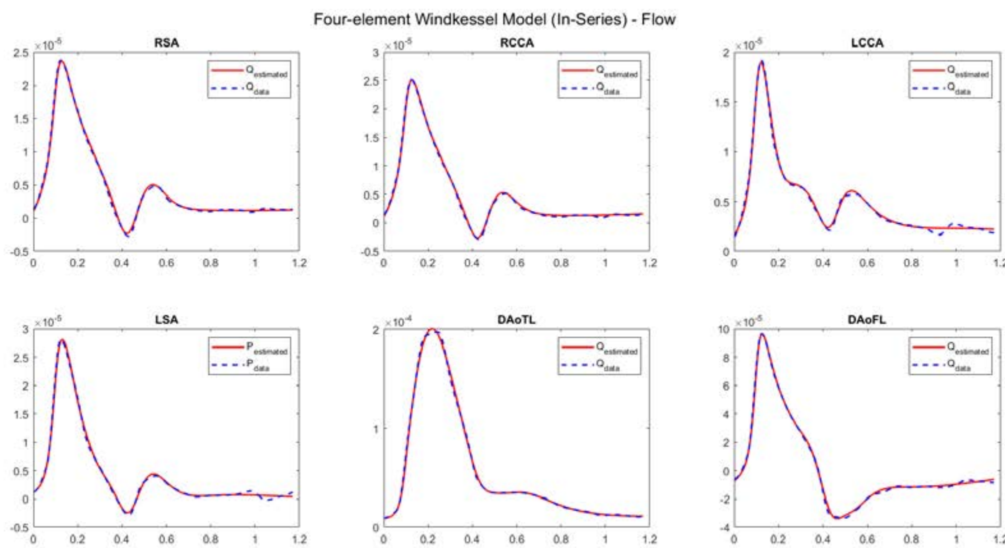

Figure 32: Predicted Flow for W4S.

The fits of all the models are evaluated by the calculation of the Root-Mean-Square difference (RMS), the Akaike Information Criterion (AIC) and the Schwarz Criterion (SC), calculated as:

$$RMS = \sqrt{SSE/(N-1)}$$
$$AIC = N \ln SSE + 2N_p$$
$$SC = N \ln SSE + N_p \ln N$$

Where $SSE = \sum_N (X_{model} - X)^2$ is the sum of squared errors, N is the number of samples and N_p the number of parameters [37]. The resulting RMS, AIC and SC for every artery of each model can be shown in Tables 10–17.

Branch	RMS ($\times 10^2$)	AIC ($\times 10^4$)	SC ($\times 10^4$)
RSA	3.93	2.22	2.23
RCCA	3.10	2.17	2.17
LCCA	2.24	2.09	2.09
LSA	3.19	2.18	2.18
DAoTL	2.96	2.16	2.16
DAoFL	2.90	2.15	2.15

Table 10: RMS, AIC, SC for W2 - Pressure.

Branch	RMS ($\times 10^{-5}$)	AIC ($\times 10^4$)	SC ($\times 10^4$)
RSA	0.35	-2.11	-2.11
RCCA	0.36	-2.11	-2.11
LCCA	0.20	-2.25	-2.24
LSA	0.39	-2.09	-2.09
DAoTL	1.98	-1.71	-1.71
DAoFL	1.75	-1.74	-1.73

Table 11: RMS, AIC, SC for W2 - Flow.

Branch	RMS ($\times 10^1$)	AIC ($\times 10^4$)	SC ($\times 10^4$)
RSA	7.38	1.83	1.84
RCCA	6.67	1.81	1.81
LCCA	4.78	1.73	1.73
LSA	6.96	1.82	1.82
DAoTL	6.96	1.82	1.82
DAoFL	5.55	1.77	1.77

Table 12: RMS, AIC, SC for W3 - Pressure.

Branch	RMS ($\times 10^{-6}$)	AIC ($\times 10^4$)	SC ($\times 10^4$)
RSA	0.26	-2.72	-2.72
RCCA	0.24	-2.74	-2.74
LCCA	0.23	-2.75	-2.75
LSA	0.34	-2.66	-2.66
DAoTL	1.50	-2.31	-2.31
DAoFL	1.61	-2.30	-2.29

Table 13: RMS, AIC, SC for W3 - Flow.

Branch	RMS ($\times 10^1$)	AIC ($\times 10^4$)	SC ($\times 10^4$)
RSA	3.35	1.65	1.65
RCCA	2.24	1.56	1.56
LCCA	7.81	1.85	1.85
LSA	2.67	1.60	1.60
DAoTL	3.30	1.65	1.65
DAoFL	3.66	1.67	1.67

Table 14: RMS, AIC, SC for W4P - Pressure.

Branch	RMS ($\times 10^{-6}$)	AIC ($\times 10^4$)	SC ($\times 10^4$)
RSA	0.27	-2.71	-2.71
RCCA	0.30	-2.69	-2.68
LCCA	0.48	-2.58	-2.57
LSA	0.32	-2.67	-2.67
DAoTL	1.75	-2.27	-2.27
DAoFL	1.90	-2.25	-2.25

Table 15: RMS, AIC, SC for W4P - Flow.

Branch	RMS ($\times 10^1$)	AIC ($\times 10^4$)	SC ($\times 10^4$)
RSA	7.47	1.84	1.84
RCCA	3.27	1.64	1.65
LCCA	2.77	1.60	1.61
LSA	3.36	1.65	1.65
DAoTL	3.75	1.68	1.68
DAoFL	3.65	1.67	1.67

Table 16: RMS, AIC, SC for W4S - Pressure.

Branch	RMS ($\times 10^{-6}$)	AIC ($\times 10^4$)	SC ($\times 10^4$)
RSA	0.27	-2.71	-2.71
RCCA	0.26	-2.72	-2.72
LCCA	0.24	-2.74	-2.73
LSA	0.37	-2.64	-2.64
DAoTL	1.80	-2.27	-2.27
DAoFL	1.21	-2.36	-2.36

Table 17: RMS, AIC, SC for W4S - Flow.

5.3 Frequency Response

5.3.1 Bode Plots

If one views the flow as the input of the arterial system and the pressure as the produced output, using the Windkessel models' equations the transfer functions for each can be obtained. A transfer function is the transfer gain from input to output and is equal to the ratio of the Laplace transform -in our case- of $P(t)$ to $Q(t)$ [38]. The resulting transfer functions for each Windkessel model are the following:

- W2:

$$G(s) = \frac{R}{sRC + 1} \tag{16}$$

1st order

- W3:

$$G(s) = \frac{sRCZ + R + Z}{sRC + 1} \tag{17}$$

1st order

- W4P:

$$G(s) = \frac{s^2RCLZ + s(LR + LZ) + RZ}{s^2RCL + s(L + RCZ) + Z} \tag{18}$$

2nd order

- W4S:

$$G(s) = \frac{s^2LCR + s(L + ZCR) + Z + R}{CRs + 1} \tag{19}$$

The numeratior's order is higher than the denominator's, making this system improper and leading to non-physical behavior.

The frequency response of a linear dynamical system, (like the Windkessel models discussed in this thesis), is the complex function $G(j\omega)$ of the real angular frequency ω.

An important tool, that is a sufficient but not necessary condition for instability, based on calculating the amplitude and phase angle for the transfer function of the system is the Bode plot [39]. It consists of two plots, where the first is the gain $A = |G(j\omega)|$ and the second the phase $\phi\angle G(j\omega)$, both against the frequency ω. While for the purpose of this thesis, all the Bode plots were created using MATLAB's `bode` function, it is important to understand how they can be calculated.

For the gain A the complex function $G(j\omega)$ of the real frequency is used, where $G(j\omega) = R(\omega) + jX(\omega)$. R is the real and X the imaginary part of G respectively. Then $A = \sqrt{R^2 + X^2}$.

Regarding the phase shift, the polar form of $G(j\omega)$ is used where, $G(j\omega) = |G(j\omega)|e^{j\phi(\omega)} = |G(j\omega)|\angle\phi(\omega)$ and $\phi(\omega) = tan^{-1}\frac{X(\omega)}{R(\omega)}$. All the above calculations were presented in the course "Automatic Control" by Dr. Konstantinos Ampountolas.

The two-element Windkessel (Figure 33) is a first-order low-pass filter since it passes low frequencies ($\omega \rightarrow 0$, $G(0) = R$) with minimal attenuation while the system dampens high frequencies (the gain is dropping). It also introduces a phase lag that increases with frequency, reaching $-90°$ asymptotically. The higher the value of the time constant τ (Table 9), the quicker the magnitude $|G(j\omega)|$ and the phase begin to drop.

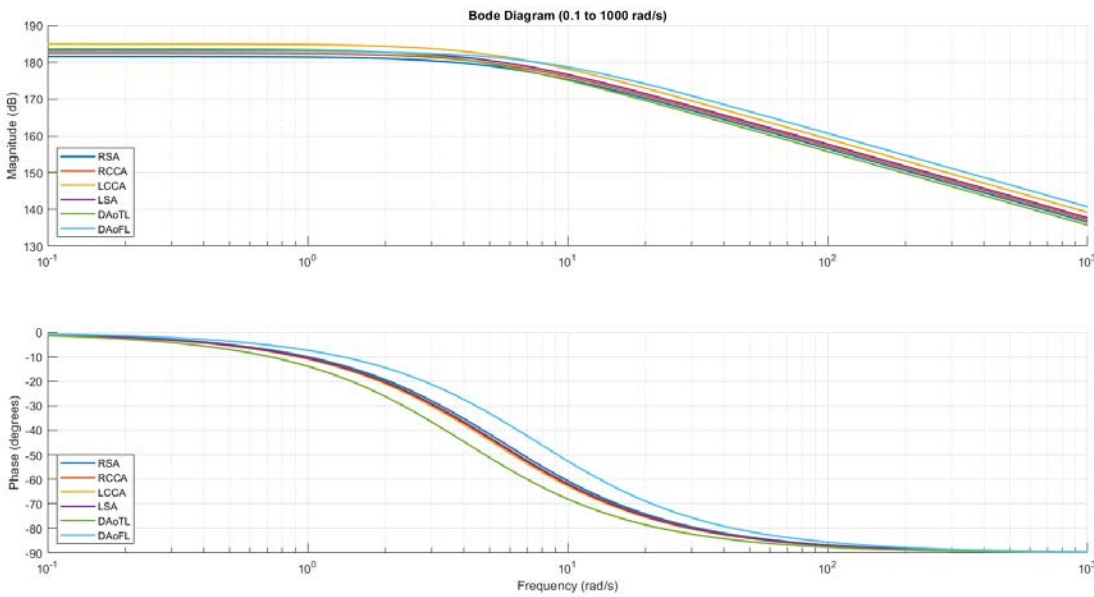

Figure 33: Bode plot for W2.

Regarding the three-element Windkessel (Figure 34), for low frequencies the gain is equal to $R + Z$ and the magnitude again drops with the same behavior according to the time constant τ like the two-element Windkessel. A difference can be observed in the phase plot where, when reaching $-90°$, it begins to climb to higher values. This behavior can be attributed to the characteristic impedance Z dominating, since there is a slower ascend (DAoTL) for low values, in contrast to higher ones.

The four-element Windkessel's (parallel) magnitude starts at $G(0) = R$ and then behaves like the rest, with only $LCCA$ deviating, due to the lower R value. The phase rises quicker due to the inductive component L, which causes a phase advance in higher frequencies, dominating the compliance (Figure 35).

Lastly, the four-element Windkessel (in-series), shows differences compared to the rest of the plots (Figure 36). While the magnitude drops for intermediate frequencies, it starts to rise at $100 - 1000 rad/s$. This is because the inductive term L, continues to dominate at higher frequencies (similar to W4P) but shows instabilities due to the different connection. For the same reason, the phase starts rising for higher values of ω.

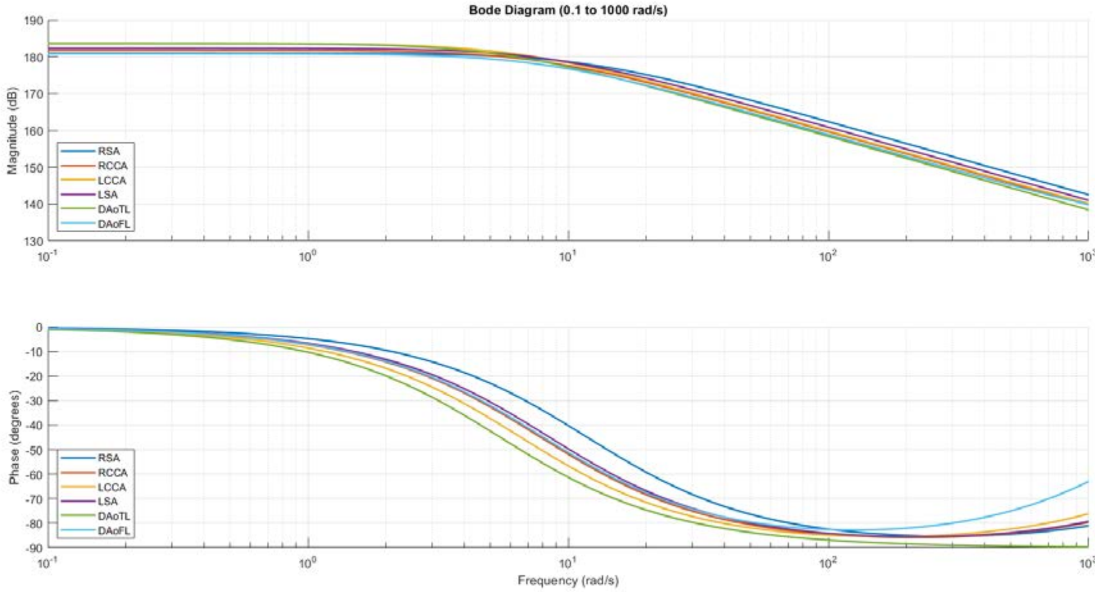

Figure 34: Bode plot for W3.

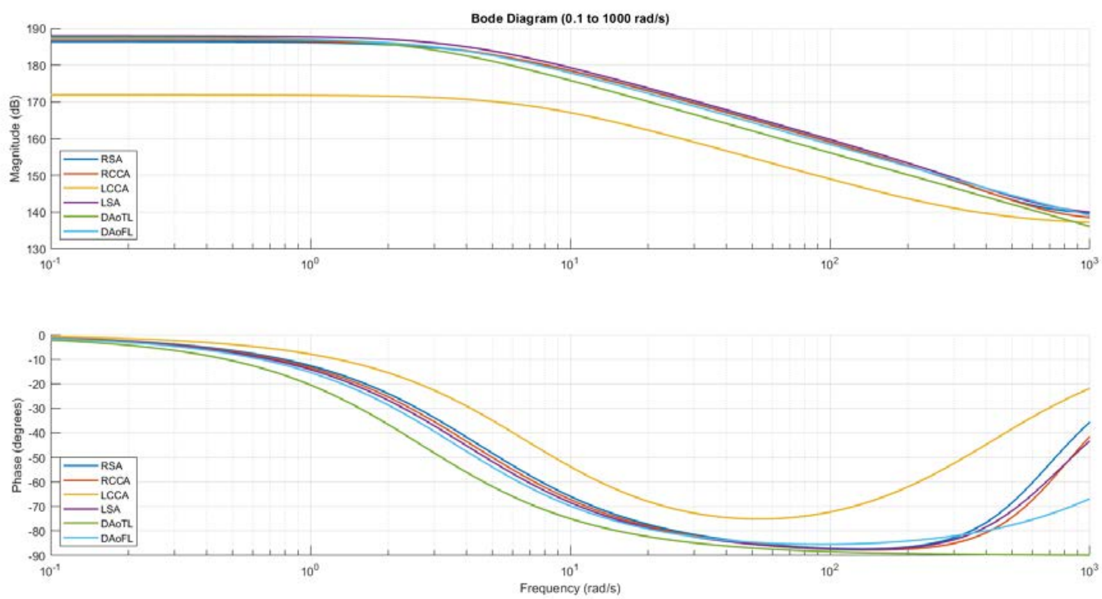

Figure 35: Bode plot for W4P.

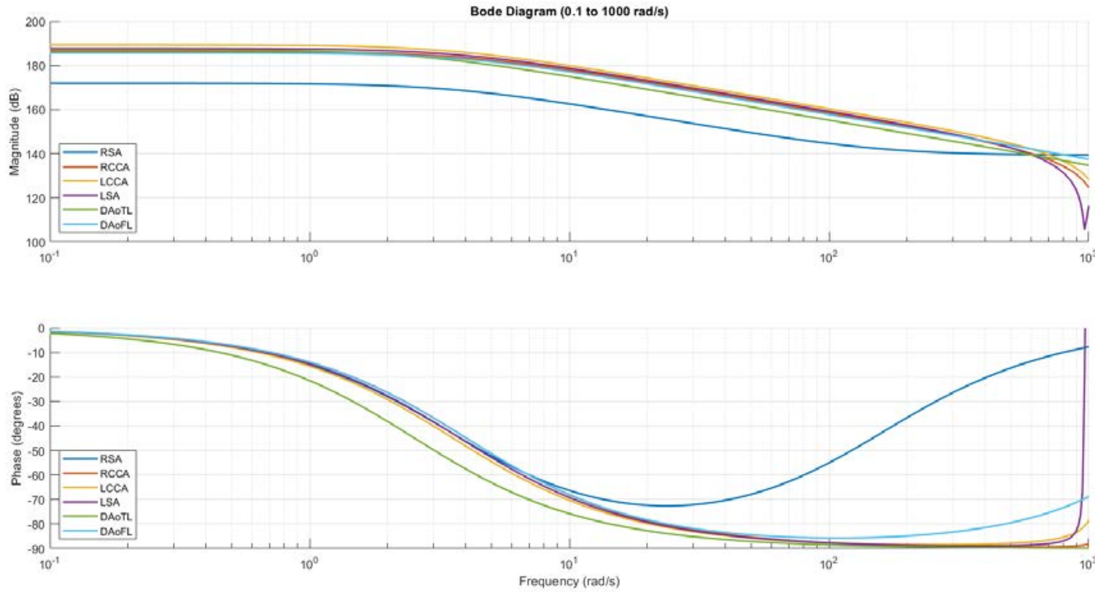

Figure 36: Bode plot for W4S.

It is important to note, that due to the nature of the system, there is no real significance investigating frequencies higher than $1000 rad/s$.

5.3.2 Input Impedance

[21] describes what input impedance is and its meaning regarding the arterial system. Impedance is the relation between pressure and flow through a linear system for sinusoidal signals. It completely describes the system at its entrance and for this reason it is called input impedance. It is derived from the pulsatile pressure and flow by applying Fourier analysis and calculating their harmonics (a pair of sine waves). For each harmonic, the ratio of amplitudes (impedance modulus) and the difference in phase angle (impedance phase angle) are calculated.

In an idealized arterial system without reflections (pressure and flow waves bouncing back towards the inlet due to changes in vessel geometry or resistance), the input impedance is equal to the characteristic impedance of the aorta; a property of the vessel (calculated by Equation 9), representing the impedance of a semi-infinite vessel where no reflections occur. These reflections travel back toward the heart and alter the pressure and flow waveforms at the aortic root.

At low frequencies the reflections at the many discontinuities (diffuse reflections) add in phase and cause the impedance to be high (large total reflection). For intermediate frequencies, the impedance modulus decreases and the phase angle is negative, showing the contribution of total arterial compliance. At higher frequencies, the local reflected waves return with different phases, canceling each other, and contribute less causing the input impedance to be close to the characteristic impedance. Analyzing multiple heartbeats and averaging the results decreases noise when plotting the impedance modulus and phase angle.

Calculating the input impedance using the Windkessel models, after having formed the transfer functions (Equations 16–19) is easy, substituting $j\omega$ for s in each equation since the analysis is again in the frequency domain. The input impedance for each model is:

- W2:

$$16 \rightarrow Z_{in} = \frac{R}{j\omega RC + 1} \tag{20}$$

- W3:

$$17 \rightarrow Z_{in} = \frac{j\omega RCZ + R + Z}{j\omega RC + 1} \tag{21}$$

- W4P:

$$18 \rightarrow Z_{in} = \frac{(j\omega)^2 RCLZ + j\omega(LR + LZ) + RZ}{(j\omega)^2 RCL + j\omega(L + RCZ) + Z} \tag{22}$$

- W4S:

$$19 \rightarrow Z_{in} = \frac{(j\omega)^2 LCR + j\omega(L + ZCR) + Z + R}{j\omega RC + 1} \tag{23}$$

After using MATLAB's `ftt` function on the pressure and flow data to calculate the "measured" input impedance it was then compared with the impedances computed by each model for all six arteries (Figures 37–48).

It is clear that the estimated impedances do not capture the measured input impedance well, especially the phase plots which have very awkward behavior. This highlights an issue related with the data used for training since pressure was obtained by a simulator while flow from in-vivo measurements. These two waveforms do not have real correlation thus producing non-realistic impedance plots. For this reason, the comparison of the measured and the estimated impedance has no meaning in our application.

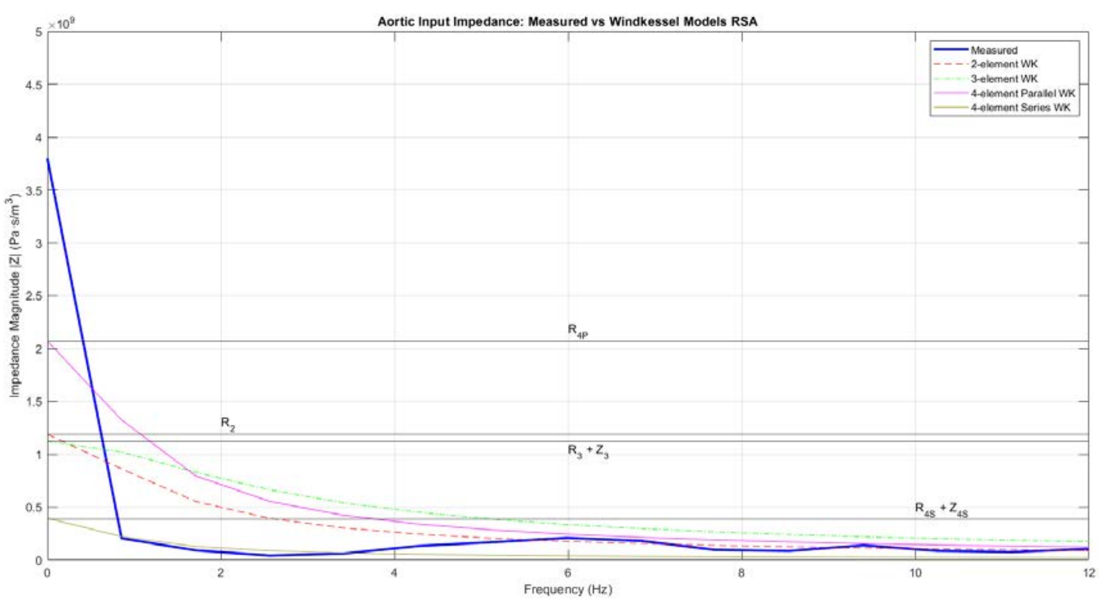

Figure 37: Input Impedance modulus for RSA.

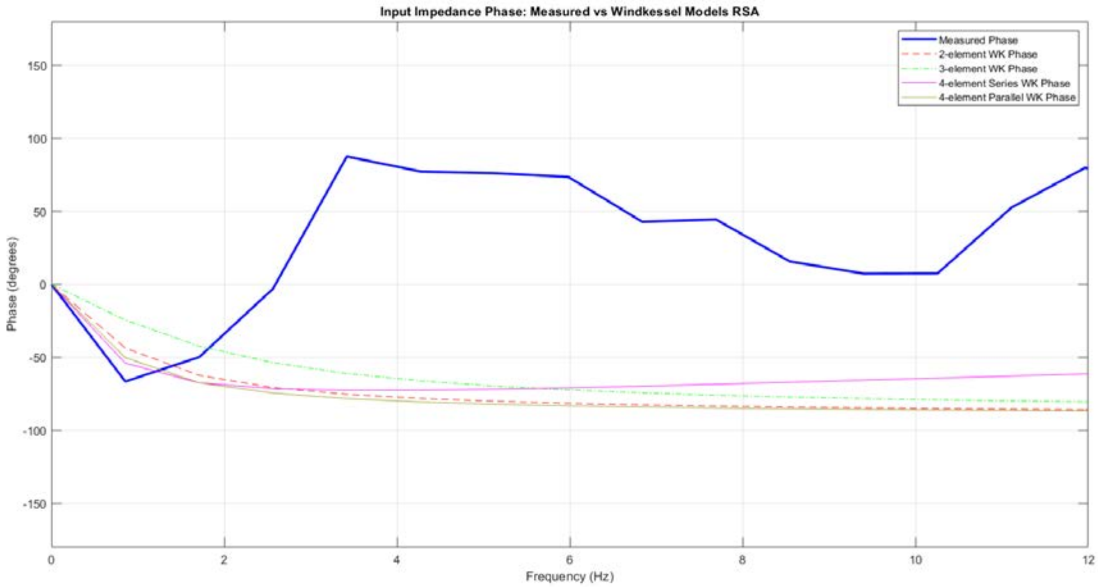

Figure 38: Input Impedance phase angle for RSA.

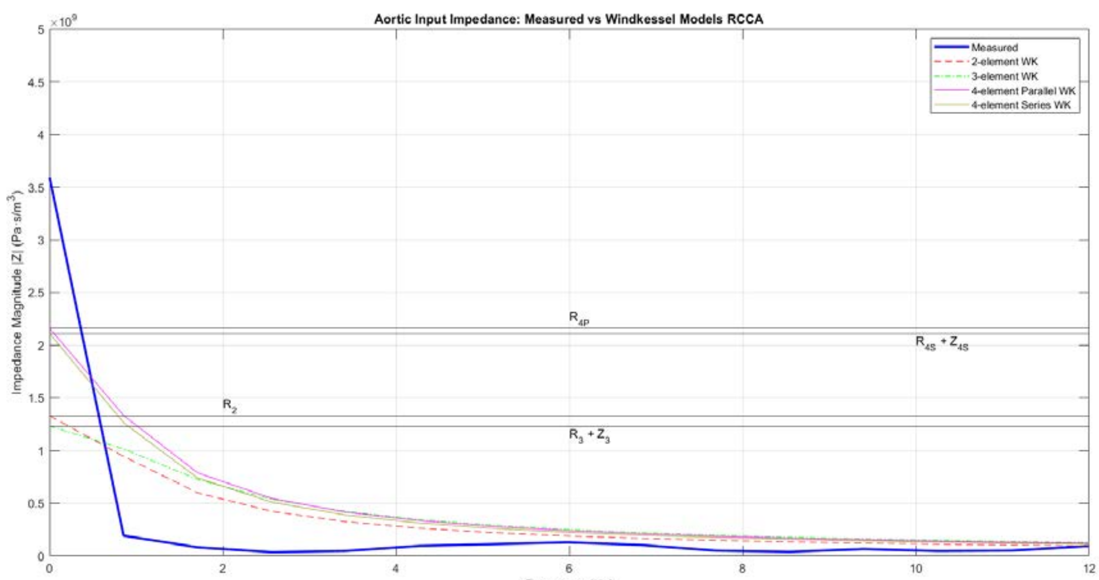

Figure 39: Input Impedance modulus for RCCA.

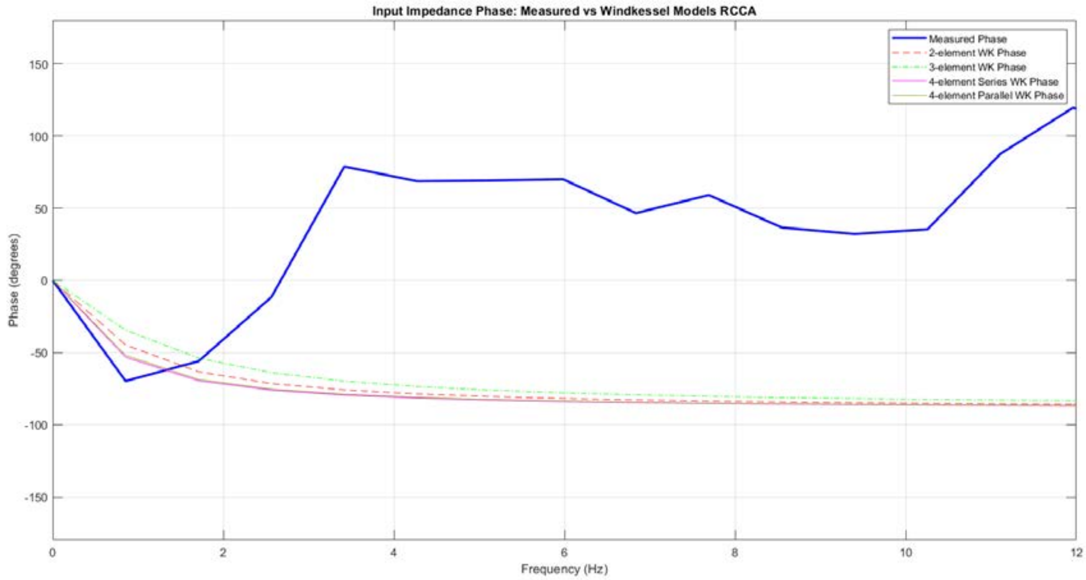

Figure 40: Input Impedance phase angle for RCCA.

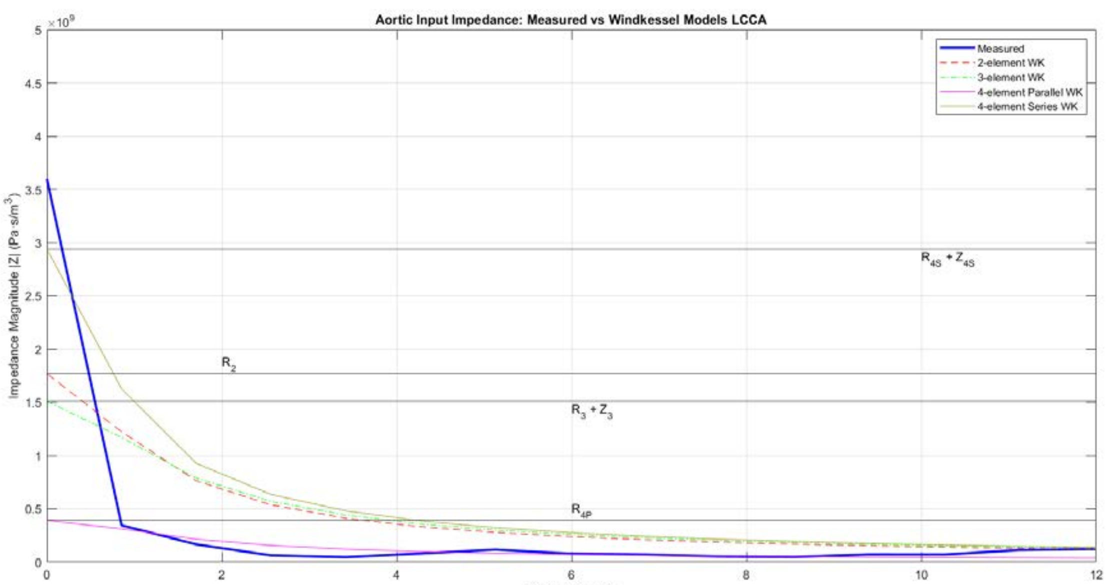

Figure 41: Input Impedance modulus for LCCA.

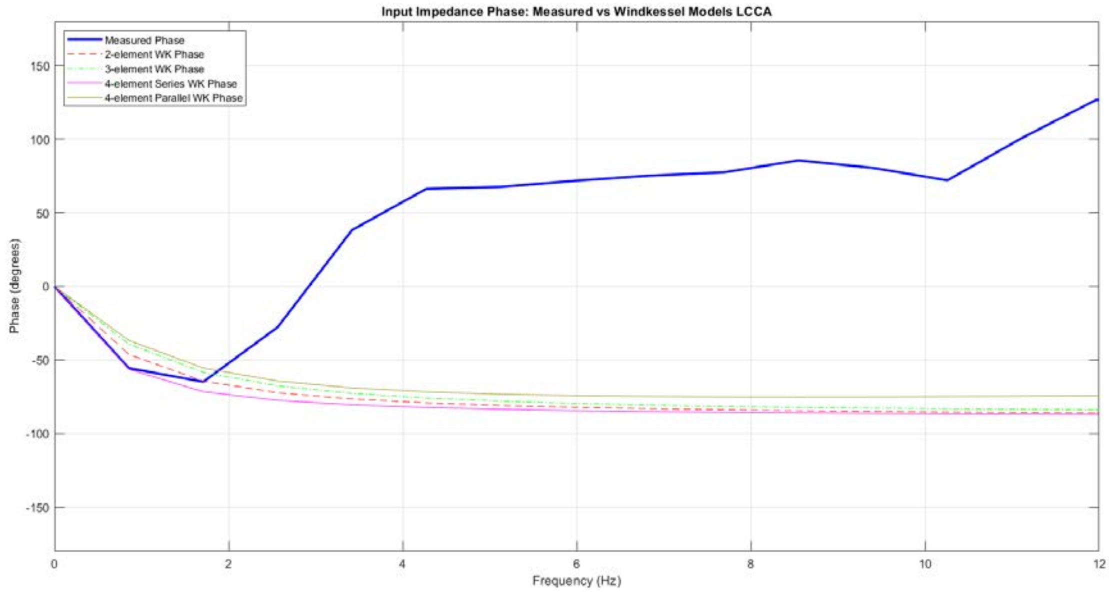

Figure 42: Input Impedance phase angle for LCCA.

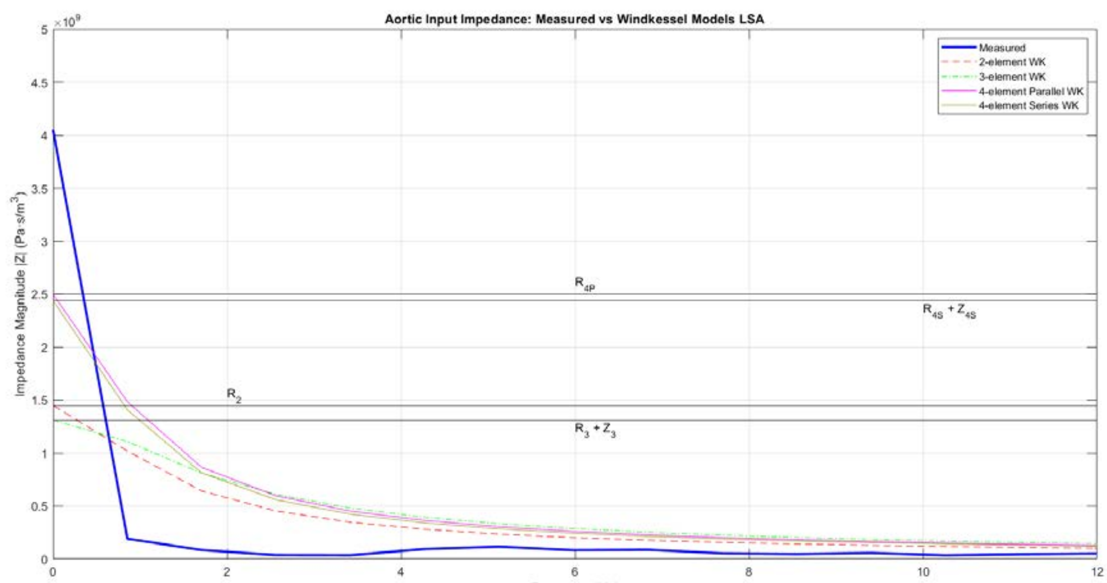

Figure 43: Input Impedance modulus for LSA.

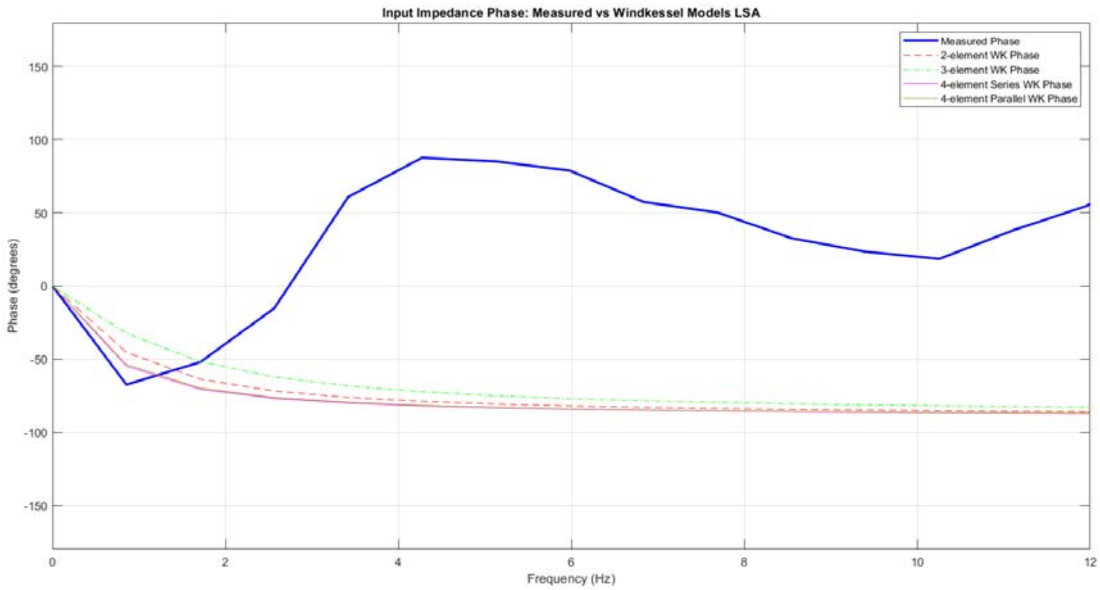

Figure 44: Input Impedance phase angle for LSA.

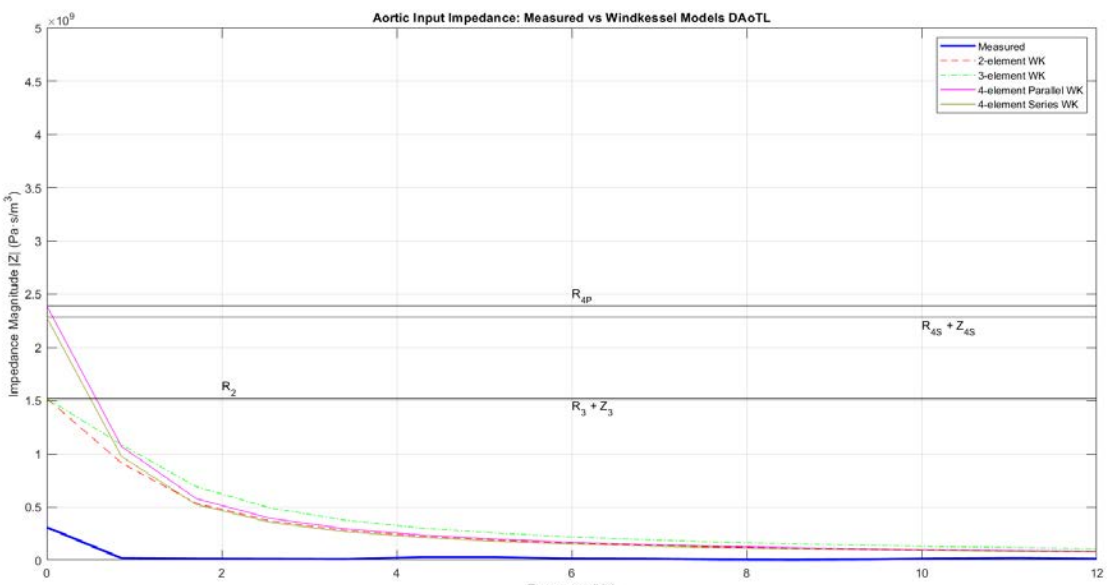

Figure 45: Input Impedance modulus for DAoTL.

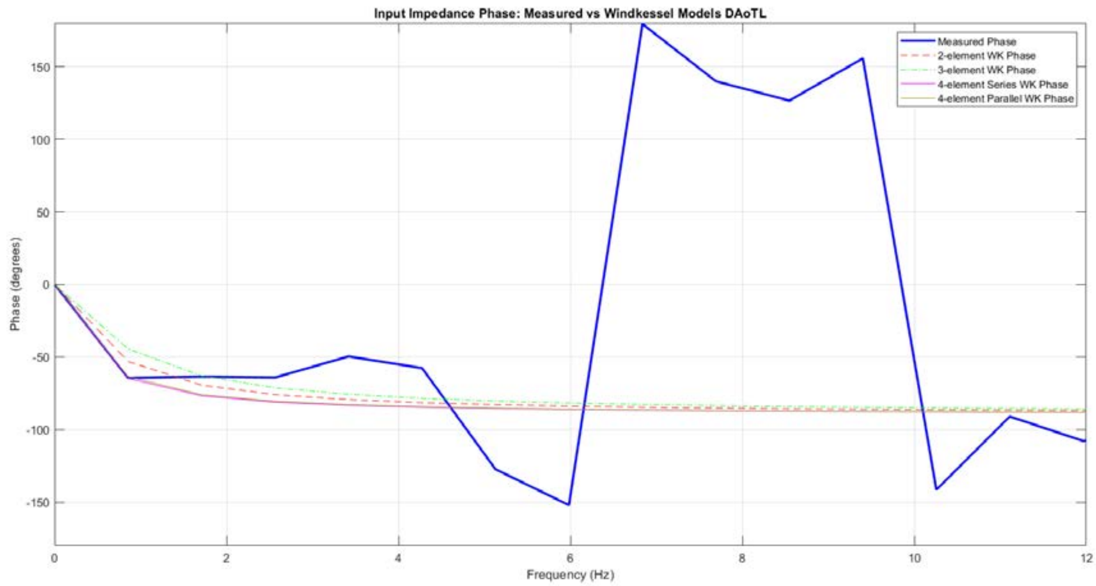

Figure 46: Input Impedance phase angle for DAoTL.

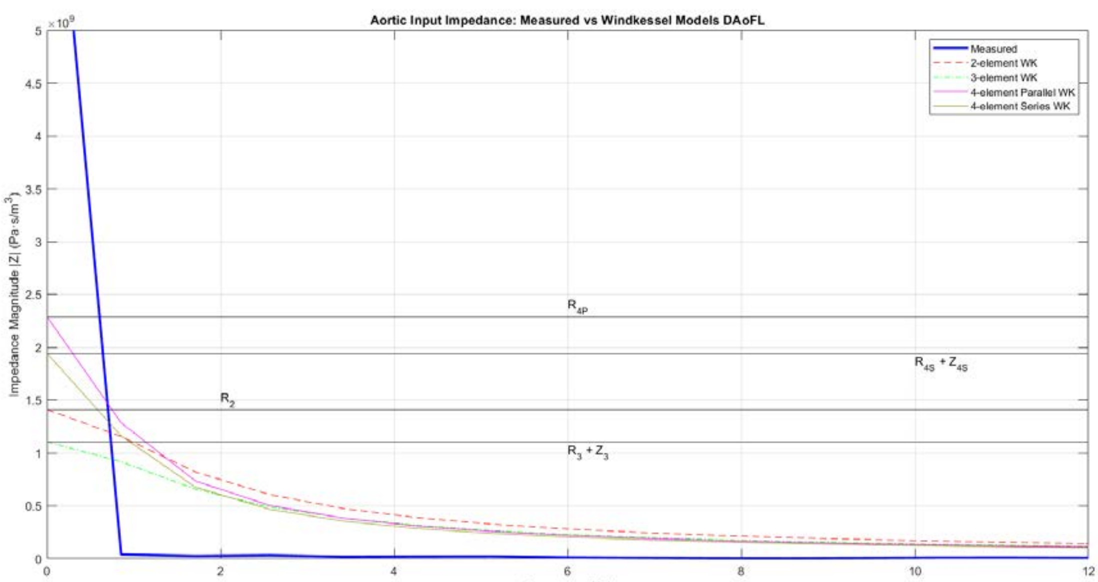

Figure 47: Input Impedance modulus for DAoFL.

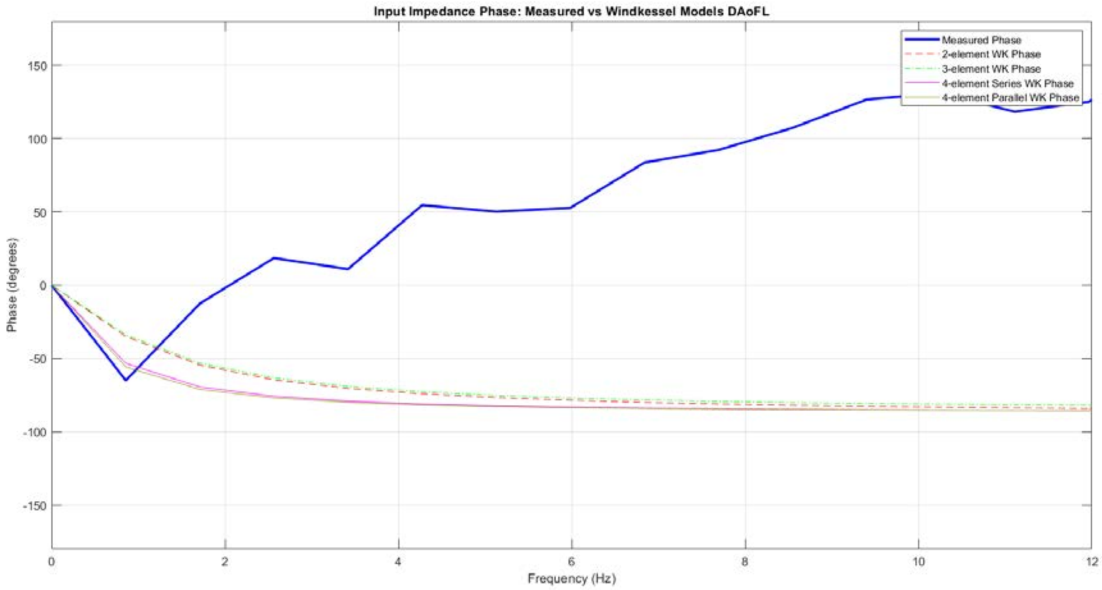

Figure 48: Input Impedance phase angle for DAoFL.

6 Discussion and Future Work

After collecting the results presented above for each aspect of the parameters' evaluation, the comparison of the four models used can be initiated. Regarding the estimated waveforms, it is clear that while the two-element Windkessel model captures the general shape, it lacks detail in the slope transitions. The three-element Windkessel shows high accuracy with low computational demand and both the four-element Windkessel models (parallel and in-series) show even higher precision, while being more complex to train. Especially for the parallel connection, convergence was not obtained for all the parameters.

The Bode plots depicted each model's behavior as was expected according to their transfer functions and the contribution of each parameter. It was also shown that the four-element Windkessel in-series had an improper transfer function as the numerator was of higher order than the denominator and behaved accordingly. Impedance calculation highlighted the mismatch between synthetic pressure and in-vivo flow data, and how it introduced inconsistencies, especially for the phase plots. No meaningful conclusion can be derived from the comparisons in Section 5.3.2. A summary of each model's behavior is shown in Table 18.

Criterion	W2	W3	W4P	W4S
Parameters	R,C	R,C,Z	R,C,Z,L	R,C,Z,L
Prediction Accuracy	Low	High	High	High
Computational Cost	Low	Moderate	High	High
Training Stability	High	High	Lower	Lower
Frequency Response	1st order	1st order	2nd order	Improper
Recommended Use	Quick Approximation	Balanced Modeling	In-depth Modeling	Rarely Recommended

Table 18: Summary Comparison of Windkessel Models.

Physics-informed neural networks have proven to be effective for inverse parameter estimation even with sparse or noisy data, enabling a non-invasive calibration of cardiovascular models using limited clinical input. In hopes to improve the proposed model, it is essential to use data better correlated. This mismatch makes the evaluation of the results troublesome and non-realistic. Also, since PINNs include numerous hyper-parameters, a different fine-tuning is another field for optimization. The neural network's architecture, the initializer and the weight distribution are just a few of the many model settings that could change and yield better results. Also, the modeling could be extended to full systemic circulation, as well as more cardiac cycles, capturing a bigger picture of the cardiovascular system. Lastly, real-time estimation using light-weight networks could be explored for faster, clinically viable applications.

References

[1] Thomas C Gasser. Aorta. *Biomechanics of Living Organs*, pages 169–191, 2017.

[2] Wilmer W Nichols, Michael O'Rourke, Elazer R Edelman, and Charalambos Vlachopoulos. *McDonald's blood flow in arteries: theoretical, experimental and clinical principles.* CRC press, 2022.

[3] Xiaomei Guo and Ghassan S Kassab. Variation of mechanical properties along the length of the aorta in c57bl/6 mice. *American Journal of Physiology-Heart and Circulatory Physiology*, 285(6):H2614–H2622, 2003.

[4] John F Jr. LaDisa, Ronak J Dholakia, C Alberto Figueroa, Irene E Vignon-Clementel, Frandics P Chan, Margaret M Samyn, Joseph R Cava, Charles A Taylor, and Jeffrey A Feinstein. Computational simulations demonstrate altered wall shear stress in aortic coarctation patients treated by resection with end-to-end anastomosis. *Congenital heart disease*, 6(5):432–443, 2011.

[5] Kwong Ming Tse, Peixuan Chiu, Heow Pueh Lee, and Pei Ho. Investigation of hemodynamics in the development of dissecting aneurysm within patient-specific dissecting aneurismal aortas using computational fluid dynamics (cfd) simulations. *Journal of biomechanics*, 44(5):827–836, 2011.

[6] Frank W Sellke, Joseph S Coselli, Thoralf M Sundt, Joseph E Bavaria, and Neel R Sodha. *Aortic Dissection and Acute Aortic Syndromes.* Springer, 2021.

[7] Christopher RH Wilbers, Clark L Carrol, and Mark A Hnilica. Optimal diagnostic imaging of aortic dissection. *Texas Heart Institute Journal*, 17(4):271, 1990.

[8] Myron W Wheat Jr and Roger F Palmer. Dissecting aneurysms of the aorta: present status of drug versus surgical therapy. *Progress in Cardiovascular Diseases*, 11(3):198–210, 1968.

[9] Isidor Kokalari, Theodhor Karaja, and Maria Guerrisi. Review on lumped parameter method for modeling the blood flow in systemic arteries. *Journal of biomedical science and engineering*, 6(1):92–99, 2013.

[10] D. Burkhoff, J. Alexander, and J. Schipke. Assessment of windkessel as a model of aortic input impedance. *American Journal of Physiology-Heart and Circulatory Physiology*, 255(4):H742–H753, 1988. PMID: 3177666.

[11] Alberto P Avolio. Multi-branched model of the human arterial system. *Medical and Biological Engineering and Computing*, 18:709–718, 1980.

[12] Yubing Shi, Patricia Lawford, and Rodney Hose. Review of zero-d and 1-d models of blood flow in the cardiovascular system. *Biomedical engineering online*, 10:1–38, 2011.

[13] Kiichi Sagawa, Reidar K Lie, and Jochen Schaefer. Translation of otto frank's paper" die grundform des arteriellen pulses" zeitschrift für biologie 37: 483-526 (1899). *Journal of molecular and cellular cardiology*, 22(3):253–254, 1990.

[14] Patrick Segers, Nikos Stergiopulos, Nico Westerhof, Patrick Wouters, Philippe Kolh, and Pascal Verdonck. Systemic and pulmonary hemodynamics assessed with a lumped-parameter heart-arterial interaction model. *Journal of engineering mathematics*, 47:185–199, 2003.

[15] Georgios Kissas, Yibo Yang, Eileen Hwuang, Walter R Witschey, John A Detre, and Paris Perdikaris. Machine learning in cardiovascular flows modeling: Predicting arterial blood pressure from non-invasive 4d flow mri data using physics-informed neural networks. *Computer Methods in Applied Mechanics and Engineering*, 358:112623, 2020.

[16] Nico Westerhof, Jan-Willem Lankhaar, and Berend E Westerhof. The arterial windkessel. *Medical & biological engineering & computing*, 47(2):131–141, 2009.

[17] Nicolaas Westerhof, GIJS Elzinga, and Pieter Sipkema. An artificial arterial system for pumping hearts. *Journal of applied physiology*, 31(5):776–781, 1971.

[18] NMJWN Stergiopulos, JJ Meister, and N Westerhof. Evaluation of methods for estimation of total arterial compliance. *American Journal of Physiology-Heart and Circulatory Physiology*, 268(4):H1540–H1548, 1995.

[19] Anirban Dutta Choudhury, Rohan Banerjee, Aniruddha Sinha, and Shaswati Kundu. Estimating blood pressure using windkessel model on photoplethysmogram. In *2014 36th annual international conference of the IEEE engineering in medicine and biology society*, pages 4567–4570. IEEE, 2014.

[20] Erik Wetterer. *Quantitative Beziehungen zwischen Stromstärke und Druck im natürlichen Kreislauf bei zeitlich variabler Elastizität des arteriellen Windkessels; Wetterer, Erik, Dr. med.* JF Lehmanns Verlag, 1940.

[21] Nicolaas Westerhof, Nikolaos Stergiopulos, Mark IM Noble, and Berend E Westerhof. *Snapshots of hemodynamics: an aid for clinical research and graduate education.* Springer, 2018.

[22] G Landes. Einige untersuchungen an elektrischen analogieschaltungen zum kreitslaufsystem. *Z Biol*, 101:418–429, 1943.

[23] Nikos Stergiopulos, Berend E Westerhof, and Nico Westerhof. Total arterial inertance as the fourth element of the windkessel model. *American Journal of Physiology-Heart and Circulatory Physiology*, 276(1):H81–H88, 1999.

[24] Roberto Burattini and Paola Oriana Di Salvia. Development of systemic arterial mechanical properties from infancy to adulthood interpreted by four-element windkessel models. *Journal of Applied Physiology*, 103(1):66–79, 2007.

[25] Huan Huang, Ming Yang, Wangfu Zang, Shunjie Wu, and Yafei Pang. In vitro identification of four-element windkessel models based on iterated unscented kalman filter. *IEEE transactions on biomedical engineering*, 58(9):2672–2680, 2011.

[26] Taco Kind, Theo JC Faes, Jan-Willem Lankhaar, Anton Vonk-Noordegraaf, and Michel Verhaegen. Estimation of three-and four-element windkessel parameters using subspace model identification. *IEEE Transactions on Biomedical Engineering*, 57(7):1531–1538, 2010.

[27] Kevin Gurney. *An introduction to neural networks*. CRC press, 2018.

[28] Chris M Bishop. Neural networks and their applications. *Review of scientific instruments*, 65(6):1803–1832, 1994.

[29] Yu-chen Wu and Jun-wen Feng. Development and application of artificial neural network. *Wireless Personal Communications*, 102:1645–1656, 2018.

[30] Maziar Raissi, Paris Perdikaris, and George E Karniadakis. Physics-informed neural networks: A deep learning framework for solving forward and inverse problems involving nonlinear partial differential equations. *Journal of Computational physics*, 378:686–707, 2019.

[31] Lu Lu, Xuhui Meng, Zhiping Mao, and George Em Karniadakis. Deepxde: A deep learning library for solving differential equations. *SIAM review*, 63(1):208–228, 2021.

[32] SMD Black, C Maclean, P Hall Barrientos, K Ritos, A McQueen, and A Kazakidi. Calibration of patient-specific boundary conditions for coupled cfd models of the aorta derived from 4d flow-mri. front bioeng biotechnol 11, 2023.

[33] Nan Xiao. *Simulation of 3-D blood flow in the full systemic arterial tree and computational frameworks for efficient parameter estimation*. Stanford University, 2014.

[34] Jordi Alastruey Arimon. *Numerical modelling of pulse wave propagation in the cardiovascular system: development, validation and clinical applications*. PhD thesis, Imperial College London (University of London), 2006.

[35] Henderi Henderi, Tri Wahyuningsih, and Efana Rahwanto. Comparison of min-max normalization and z-score normalization in the k-nearest neighbor (knn) algorithm to test the accuracy of types of breast cancer. *International Journal of Informatics and Information Systems*, 4(1):13–20, 2021.

[36] Jordi Alastruey, Tiziano Passerini, Luca Formaggia, and Joaquim Peiró. Physical determining factors of the arterial pulse waveform: theoretical analysis and calculation using the 1-d formulation. *Journal of Engineering Mathematics*, 77:19–37, 2012.

[37] Patrick Segers, ER Rietzschel, ML De Buyzere, N Stergiopulos, N Westerhof, LM Van Bortel, Thierry Gillebert, and PR Verdonck. Three-and four-element windkessel models: assessment of their fitting performance in a large cohort of healthy middle-aged individuals. *Proceedings of the Institution of Mechanical Engineers, Part H: Journal of Engineering in Medicine*, 222(4):417–428, 2008.

[38] Gene F Franklin, J David Powell, Abbas Emami-Naeini, and J David Powell. *Feedback control of dynamic systems*, volume 4. Prentice hall Upper Saddle River, 2002.

[39] Jürgen Hahn, Thomas Edison, and Thomas F Edgar. A note on stability analysis using bode plots. *Chemical Engineering Education*, 35(3):208–211, 2001.